JVI Journals.ASM.org

Release of Severe Acute Respiratory Syndrome Coronavirus Nuclear Import Block Enhances Host Transcription in Human Lung Cells

Amy C. Sims,[a] Susan C. Tilton,[d] Vineet D. Menachery,[a] Lisa E. Gralinski,[a] Alexandra Schäfer,[a] Melissa M. Matzke,[d] Bobbie-Jo M. Webb-Robertson,[d] Jean Chang,[e] Maria L. Luna,[d] Casey E. Long,[a] Anil K. Shukla,[d] Armand R. Bankhead III,[f] Susan E. Burkett,[c] Gregory Zornetzer,[e]* Chien-Te Kent Tseng,[g] Thomas O. Metz,[d] Raymond Pickles,[b,c] Shannon McWeeney,[f] Richard D. Smith,[d] Michael G. Katze,[e,h] Katrina M. Waters,[d] Ralph S. Baric[a,b]

Departments of Epidemiology[a] and Microbiology and Immunology[b] and Cystic Fibrosis Center,[c] University of North Carolina at Chapel Hill, Chapel Hill, North Carolina, USA; Pacific Northwest National Laboratory, Richland, Washington, USA[d]; Department of Microbiology, School of Medicine, University of Washington, Seattle, Washington, USA[e]; Oregon Health Sciences University, Portland, Oregon, USA[f]; University of Texas Medical Branch, Department of Microbiology and Immunology, Galveston, Texas, USA[g]; Washington National Primate Research Center, University of Washington, Seattle, Washington, USA[h]

The severe acute respiratory syndrome coronavirus accessory protein ORF6 antagonizes interferon signaling by blocking karyopherin-mediated nuclear import processes. Viral nuclear import antagonists, expressed by several highly pathogenic RNA viruses, likely mediate pleiotropic effects on host gene expression, presumably interfering with transcription factors, cytokines, hormones, and/or signaling cascades that occur in response to infection. By bioinformatic and systems biology approaches, we evaluated the impact of nuclear import antagonism on host expression networks by using human lung epithelial cells infected with either wild-type virus or a mutant that does not express ORF6 protein. Microarray analysis revealed significant changes in differential gene expression, with approximately twice as many upregulated genes in the mutant virus samples by 48 h postinfection, despite identical viral titers. Our data demonstrated that ORF6 protein expression attenuates the activity of numerous karyopherin-dependent host transcription factors (VDR, CREB1, SMAD4, p53, EpasI, and Oct3/4) that are critical for establishing antiviral responses and regulating key host responses during virus infection. Results were confirmed by proteomic and chromatin immunoprecipitation assay analyses and in parallel microarray studies using infected primary human airway epithelial cell cultures. The data strongly support the hypothesis that viral antagonists of nuclear import actively manipulate host responses in specific hierarchical patterns, contributing to the viral pathogenic potential *in vivo*. Importantly, these studies and modeling approaches not only provide templates for evaluating virus antagonism of nuclear import processes but also can reveal candidate cellular genes and pathways that may significantly influence disease outcomes following severe acute respiratory syndrome coronavirus infection *in vivo*.

Novel research strategies are needed to elucidate the complex virus-host interaction networks that regulate viral pathogenesis and to provide rapid response strategies for control of newly emerging viral pathogens. Prior to 2003, human coronaviruses were categorized as mildly virulent upper respiratory pathogens; however, severe acute respiratory syndrome coronavirus (SARS-CoV) infection results in high mortality rates (~10%) (1, 2). SARS-CoV emerged suddenly from zoonotic reservoirs and rapidly circumnavigated the globe in 2003 (3–8). The SARS-CoV positive-stranded RNA genome encodes a variety of novel genes that do not exist in other human coronaviruses, which likely contributes to the alteration of virulence and disease severity (9). In our study, a systems biological approach was used to examine the consequences of antagonizing karyopherin-dependent nuclear importation during SARS-CoV infection.

Signal-mediated macromolecular transport between the cytoplasm and nucleus is an integral part of cellular processes, including gene expression, signal transduction, development of antiviral states, and cell cycle progression. Highly pathogenic RNA viruses, including SARS-CoV, enteroviruses, Ebola virus, human immunodeficiency virus, cardioviruses, and Nipah viruses, encode proteins that antagonize nuclear importation processes, suggesting a common modality for regulating viral pathogenesis and disease outcomes across disparate virus families (10–14). Interestingly, the consequences of viral antagonism on host nuclear import and mRNA expression have not been carefully evaluated using genomic-based strategies. Rather, elegant reductionist approaches have demonstrated targeted antagonism of innate immune signaling pathways, typically involving interferon (IFN) regulatory factor 7 (IRF-7) and STAT transcription factors (15–20). Reflecting this approach, the interferon antagonist activity of the SARS-CoV ORF6 protein has been demonstrated to mediate its function by binding to the nuclear importation chaperone protein karyopherin. ORF6 protein binds specifically to karyopherin α2, trapping the import factor on intracellular membranes, where the complex then sequesters karyopherin β1 (17), preventing nuclear transportation of cargo into the host cell nucleus (see Fig. 1A). As karyopherin β1 is essential for all nuclear import by karyopherin α proteins, depletion of this factor may dramatically reduce or

Received 17 October 2012 Accepted 17 January 2013
Published ahead of print 30 January 2013
Address correspondence to Amy C. Sims, sims0018@ad.unc.edu.
* Present address: Gregory Zornetzer, Institute for Systems Biology, Seattle, Washington, USA.
A.C.S. and S.C.T. contributed equally to this article.
Supplemental material for this article may be found at http://dx.doi.org/10.1128/JVI.02520-12.

doi:10.1128/JVI.02520-12

alter the transport of other cargo by karyopherin-based transport mechanisms (21). We hypothesized that the ORF6 protein may actively manipulate the translocation of multiple transcription factors, coordinately modulating the levels of host transcription during infection.

Using SARS-CoV as a model system, we investigated whether the ORF6 accessory protein mediated a specific or more general block of karyopherin-mediated nuclear translocation and host gene expression. We identified a cluster of genes that are uniquely upregulated during infection with a mutant SARS-CoV strain that does not express ORF6 protein. Our data showed that ORF6 protein expression effectively ablates the activity of numerous karyopherin-dependent host transcription factors that are critical for establishing antiviral responses and regulating other key host responses during virus infection. The transcription factors identified in these studies (vitamin D receptor [VDR], cyclic AMP receptor binding protein 1 [CREB1], Oct3/4, hypoxia-inducible factor α2 [HIFα2]-Epas, p53, and SMAD4) play important roles in the regulation of a variety of cellular processes, including transforming growth factor beta induction, maintenance of normal lung cell functions, prevention of lung disease phenotypes, and proper immune cell functions (21–29). Finally, we verified our hypothesis that the upregulation of nuclear translocation attenuates viral pathogenesis with both *in vitro* and *in vivo* studies. Together, these data suggest that the ORF6 protein mediates the establishment of an intracellular environment that enhances SARS-CoV replication later in infection by suppressing host antiviral and innate immune expression cascades. In addition, these studies suggest that other viral nuclear import antagonists will also mediate pleiotropic alterations in host gene expression during infection, potentially leading to broad-based strategies for intervention and control of viral pathogenesis *in vivo*.

MATERIALS AND METHODS

Data dissemination. Raw microarray data have been deposited in the National Center for Biotechnology Information (NCBI) Gene Expression Omnibus database (30) and are accessible through the GEO series under accession number GSE33267 (http://www.ncbi.nlm.nih.gov/geo/query/acc.cgi?acc = GSE33267). Raw proteomics data corresponding to peptide identifications used to populate the AMT tag database are available at the PRoteomics IDEntification (PRIDE) database (http://www.ebi.ac.uk/pride/) under the project name "A Systems Biology Approach to Emerging Respiratory Viral Diseases" in the PRIDE Public Projects folder and corresponding to PRIDE accession numbers 19877 to 19890. The raw quantitative proteomics data can be accessed at the Pacific Northwest National Laboratory (PNNL) Biological Mass Spectrometry (MS) Data and Software Distribution Center (http://omics.pnl.gov/) in the Systems Virology Contract Data folder within the Browse Available Data folder. All data sets and associated metadata have been submitted to the Virus Pathogen Resource (ViPR; http://www.viprbrc.org). Additional details from this study and similar studies can be accessed through the Systems Virology website (http://www.systemsvirology.org).

Cells and viruses. Infections for microarray and proteomics analyses and validation studies were performed in a clonal population of Calu3 cells (human lung adenocarcinoma cells) sorted for high levels of expression of the SARS-CoV cellular receptor angiotensin-converting enzyme 2 (ACE2), referred to as Calu3 2B4 cells (31). Calu3 2B4 cells were grown in minimal essential media (MEM; Invitrogen-Gibco) containing 20% fetal bovine serum (HyClone) and 1% antibiotic-antimycotic mixture (Invitrogen-Gibco). Viral titration assays were performed in Vero E6 cells. Vero E6 cells were maintained in MEM (Invitrogen-Gibco) containing 10% fetal clone II (HyClone) and 1% antibiotic-antimycotic (Invitrogen-Gibco).

Human tracheobronchial epithelial cells were obtained from airway specimens resected from patients undergoing surgery under University of North Carolina Institutional Review Board-approved protocols by the Cystic Fibrosis Center Tissue Culture Core. Primary cells were expanded to generate passage 1 cells, and passage 2 cells were plated at a density of 2.5×10^5 cells per well on permeable Transwell-COL (12-mm-diameter) supports. Human airway epithelium (HAE) cultures were generated by provision of an air-liquid interface for 6 to 8 weeks to form well-differentiated, polarized cultures that resembled *in vivo* pseudostratified mucociliary epithelium (32).

Wild-type infectious clone-derived SARS-CoV (icSARS-CoV) and icSARS-CoV ΔORF6 and their corresponding MA15 mouse-adapted variants were derived from the Baric laboratory's infectious clone constructs as previously described (see Section S1 and Fig. S1 in the supplemental material) (9, 33, 34). Briefly, genome fragments were amplified in *Escherichia coli*, excised from plasmids by restriction digestion, ligated, and purified prior to *in vitro* transcription reactions to synthesize full-length genomic RNA, which was transfected into Vero E6 cells. The media from transfected cells were harvested and served as seed stocks for subsequent experiments. Viral genomes were confirmed by sequence analyses prior to use in any experiments. All work was performed in a biosafety level 3 facility supported by redundant fans.

Real-time PCR quantification of viral genomic and subgenomic RNA species. Relative quantities of viral genomic or subgenomic mRNA were determined by quantitative real-time PCR (qRT-PCR). First-strand cDNA synthesis was performed using 500 ng of total RNA and ThermoScript reverse transcriptase (Invitrogen) according to the manufacturer's protocol. The qPCR assay was performed using a SYBR green kit (Applied Biosystems, Carlsbad, CA) with specific primers for the different RNA species, according to the manufacturer's standard protocol. Relative RNA quantities were determined using the comparative threshold cycle (C_T) method, with human RPL14R2 serving as the endogenous reference and mock-infected samples serving as the calibrators. Primer sequences are available upon request.

icSARS-CoV and icSARS-CoV ΔORF6 infection of Calu3 2B4 cells and processing for microarray and proteomic analysis. To determine the pattern of differential gene expression or protein expression for icSARS-CoV-infected, icSARS-CoV ΔORF6-infected, and mock-infected cells, Calu3 2B4 cells were plated in triplicate under each condition at each time point, washed prior to infection, infected at a multiplicity of infection of 5 (MOI 5), and incubated at 37°C for 40 min. The inoculum was removed, cells were washed 3 times with 1× phosphate-buffered saline (PBS), and then fresh medium was added prior to time zero. For both microarray and proteomic analyses, at 0, 3, 7, 12, 24, 30, 36, 48, 54, 60, and 72 h postinfection, medium was collected to determine viral titers at each time point for each well and cells were either washed in 1× PBS and then harvested in TRIzol (Invitrogen) and stored at −80°C (for RNA) or washed 3 times in cold 150 mM ammonium bicarbonate buffer, lysed for 15 min in 8 M urea, and stored at −80°C (for protein).

Infection of primary HAE cell cultures. Infection of HAE cultures with icSARS-CoV and icSARS-CoV ΔORF6 was performed as previously described by our group (35–37). Briefly, triplicate cultures were washed with 1× PBS, and 200 μl of mock, icSARS-CoV, and icSARS-CoV ΔORF6 inocula was added to the apical surface. Cultures were incubated at 37°C for 2 h; the inoculum was removed, and unbound viruses were removed by washing three times with 1× PBS. Apical wash samples were harvested to analyze viral growth kinetics at 2, 24, 48, and 72 h postinfection and were assayed by plaque assay in Vero E6 cells (36).

RNA isolation, microarray processing, and identification of differentially expressed transcripts. RNA isolation from Calu3 2B4 cells and the subsequent microarray processing and identification of differentially expressed transcripts were performed as described previously (38). All probes were required to pass Agilent quality control (QC) flags for all

replicates of at least one infection time point (33,631 probes passed). Differential expression was determined by comparing icSARS-CoV- and icSARS-CoV ΔORF6-infected replicates to mock-infected replicates for each time point, based on a linear model fit for each transcript. Criteria for differential expression were an absolute $\log_2$-fold change of 1.5 and a false discovery rate (FDR)-adjusted *P* value of <0.05 for a given time point. Differential expression was also calculated directly between icSARS-CoV and icSARS-CoV ΔORF6 for each time point by using the criteria of a 2-fold change and an FDR-adjusted *P* value of <0.05. Significant transcript values were transformed for clustering and network analysis to the fold change ($\log_2$) of icSARS-CoV- or icSARS-CoV ΔORF6-infected samples compared to time-matched mock-infected samples.

To process primary HAE samples, both the apical and basolateral surfaces of the cultures were washed 3 times in 1× PBS and stored at −80°C in RNAlater (Ambion/Invitrogen). To isolate total RNA, each membrane was washed twice with 500 μl of 4 M guanidinium thiocynate, 25 mM sodium citrate, 0.5% Sarkosyl, 0.1 M 2-mercaptoethanol. The washes were combined and, following shearing of the DNA, total RNA was isolated through phenol-chloroform extraction. The RNA was further purified using Qiagen RNeasy minicolumns per the manufacturer's instructions (38). Equivalent amounts of RNA from three biological replicates from each condition were pooled. Microarray analysis was performed as previously described (39) using Agilent 4x44K whole human gene expression microarrays.

Functional enrichment and transcription factor analysis. Functional enrichment statistics and network analysis were determined using DAVID (40, 41) and Metacore (GeneGo, St. Joseph, MI) to identify the most significant processes affected by infection. The DAVID functional annotation tool utilizes the Fisher exact test to measure gene enrichment in Gene Ontology (GO) biological process category terms for significant genes compared to background, which included all genes on the Agilent platform that passed the QC criteria. To identify major transcriptional regulators whose nuclear import is controlled by karyopherins, the statistical Interactome tool in MetaCore was used to measure the interconnectedness of genes in the experimental data set relative to all known interactions in the background data set. Statistical significance of overconnected interactions was calculated using a hypergeometric distribution, where the *P* value represented the probability of a particular mapping arising by chance for experimental data compared to the background (42). In order to determine the consequence of removal of the nuclear import block in SARS-ΔORF6 infection, significantly overconnected transcription factors were filtered for those whose transport is regulated by karyopherins in the cell. Networks were constructed in MetaCore for experimental data by using an algorithm that identified the shortest path to directly connect nodes in the data set to transcription factors. Network visualizations were created in MetaCore or Cytoscape (43).

Proteomic processing and analysis. The detailed proteomic methodology, including sample preparation, processing, and analysis methods, are provided in Section S2 of the supplemental material. Cell lysates were trypsin digested and fractionated by strong cation exchange as previously described (44, 45). A novel accurate mass and time (AMT) tag database (46) for virus-infected Calu3 2B4 cells was generated by liquid chromatography-tandem mass spectrometry (LC-MS/MS) analysis (44, 47), using combined aliquots of the icSARS-CoV-, icSARS-CoV ΔORF6-, and mock-infected samples. Following AMT tag database generation, LC-MS analyses were performed on all icSARS-CoV-, icSARS-CoV ΔORF6-, and mock-infected samples to generate quantitative data, using identical chromatographic and electrospray conditions as for LC-MS/MS analyses. The LC system was interfaced to an Exactive mass spectrometer (ThermoScientific), and the temperature of the heated capillary and the electrospray ionization voltage were 250°C and 2.2 kV, respectively. Data were collected over the mass range 400 to 2,000 *m/z*. Quantitative LC-MS data sets were processed using the PRISM data analysis system (48), which is a series of software tools developed in-house (e.g., Decon2LS [49] and VIPER [50], which is freely available at http://ncrr.pnl.gov/software/). Individual steps in this data processing approach are reviewed in reference 46. The peak intensity values (i.e., abundances) for the final peptide identifications were processed in a series of steps using MatLab R2010b, including quality control (51, 52), normalization (53), and quantification to protein level (54). Comparative statistical analyses of time-matched mock-infected with icSARS-CoV- and icSARS-CoV ΔORF6-infected samples was performed using a Dunnett adjusted *t* test to assess differences in protein average abundance, and a G-test was used to assess associations among factors due to the presence/absence of a response (51).

ChIP and real-time PCR. Chromatin immunoprecipitation (ChIP) analysis was performed by using the ChIP assay kit (Millipore). Briefly, Calu3 2B4 cells were infected with icSARS-CoV or icSARS-CoV ΔORF6 or mock infected, as described above, and harvested at 0, 24, and 48 h postinfection. Sonication conditions were chosen to produce the desired size distribution of chromatin, between 200 and 1,000 bp. Samples were then immunoprecipitated with anti-CREB antibody (clone aa5-24; Millipore), anti-VDR antibody (clone ab3508; Abcam), or an anti-mouse IgG (Jackson Laboratory) as a control. To verify the presence of a particular promoter fragment following ChIP, qRT-PCR was performed. Response-specific promoter regions of MMP19, CDKN1A, and MCL-1 (identified as target genes downstream of CREB or VDR) were chosen and amplified by using the following primers: MMP19_f, TCT CCC ACC AAT ACC AGC AGT TCA; MMP19_r, GGA TAC TCG GGA GGG TGG ACG TAG; CDKN_f, TCT TGG ATT GAG GAA CAG GCA ATG; CDKN_r, TCC CAA CAA ACA AGG GGT GGT T; MCL1_f, AGC CTG TTT GGT GGT GTC TTC ACA; MCL1_r, GAG ATG GGG TTT TCA CGA TGT TGG. To determine the levels (relative fold enrichment) of immunoprecipitated chromatin (specific promoter region), the C_T values were analyzed by the standard curve method, and each sample was normalized to the appropriate IgG sample and to the corresponding time-matched mock sample (55). Data presented are the means ± standard errors of means for triplicate samples.

Infection of C57BL/6J mice with icSARS-CoV or icSARS-CoV ΔORF6. Female C57BL/6J mice (B6; 20-week-old mice from Jackson Laboratories) were anesthetized with a ketamine (1.3 mg/mouse)–xylazine (0.38 mg/mouse) mixture administered intraperitoneally in a 50-μl volume. Each mouse was intranasally inoculated with 10^5 PFU wild-type icSARS-CoV mouse-adapted virus or icSARS-CoV ΔORF6 mouse-adapted backbone diluted in PBS in a volume of 50 μl. Mice were weighed daily, and at 1, 2, 4, and 7 days postinfection, 5 animals from each infection group were euthanized and the lungs were removed to determine viral titers. The large, lower lobe of the right lung was homogenized in 1 ml of sterile PBS with glass beads by using a Magnalyser (Roche) at 6,000 rpm for 60 s. Aliquots of 200 μl of lung homogenate were plated on Vero E6 cells in serial 10-fold dilutions to determine virus titers. All mice were housed using individually ventilated Sealsafe cages and the SlimLine system (Tecniplast, Exton, PA) under biosafety level 3 conditions. Experimental protocols were reviewed and approved by the Institutional Animal Care and Use Committee of the University of North Carolina, Chapel Hill.

RESULTS

icSARS-CoV and icSARS-CoV ΔORF6 growth kinetics in human lung cells. To determine if deletion of the SARS-CoV ORF6 gene caused a specific or more general effect on host transcription following the release of the block on karyopherin-mediated nuclear import, Calu3 2B4 cells were infected with icSARS-CoV or icSARS-CoV ΔORF6 at a high MOI (MOI of 5) to minimize paracrine signaling effects in uninfected cells. Medium, total RNA, and protein were harvested at 0, 3, 7, 12, 24, 36, 48, 54, 60, and 72 h postinfection. Serial dilutions of the medium samples were generated to determine viral titers, and the results for six replicate infections, graphed as the PFU per ml, are shown in Fig. 1B. For both icSARS-CoV and icSARS-CoV ΔORF6, viral titers increased by 4

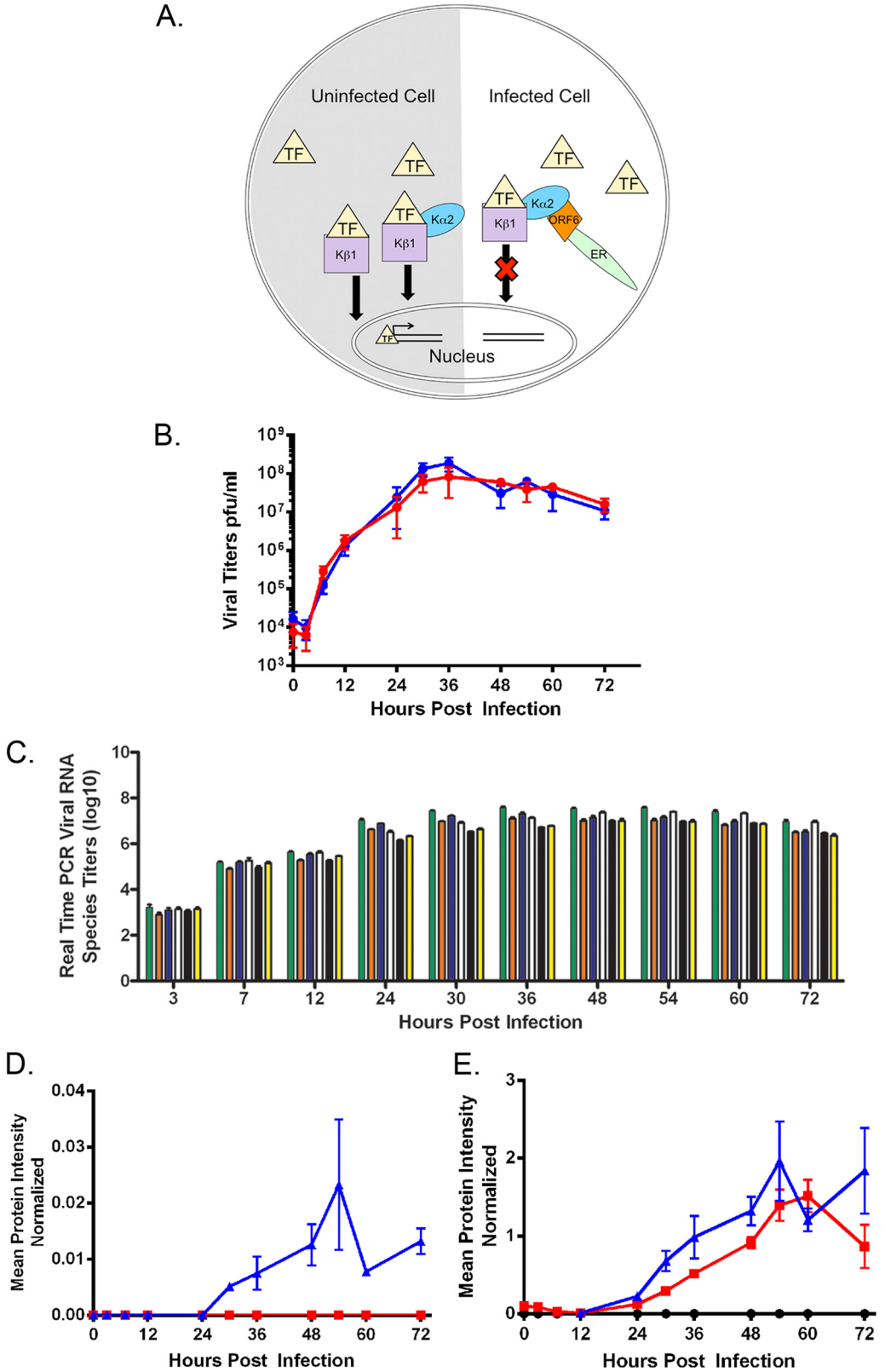

FIG 1 ORF6 function and replication kinetics in Calu3 2B4 cells. (A) Function of the interferon antagonist ORF6 protein in SARS-CoV infection. The diagram is a schematic representation of the block of nuclear translocation of the karyopherins induced by the SARS-CoV interferon antagonist, ORF6 protein. The ORF6 protein sequesters karyopherin α2 and β1 on the cytoplasmic face of the endoplasmic reticulum in infected cells, preventing nuclear translocation of many factors, including transcription factors (TF) that require karyopherins for nuclear entry, preventing transcription of downstream genes. Kα2, karyopherin α2; Kβ1, karyopherin β1; ER, endoplasmic reticulum. (B and C) Triplicate wells of Calu3 2B4 human lung cells were infected with either icSARS-CoV or

logs by 30 h postinfection, with peak titers reaching ~10^8 at 36 h postinfection (Fig. 1B). No significant difference in titer between icSARS-CoV and icSARS-CoV ΔORF6 was detected at any time postinfection, and a similar percentage of cells was infected (data not shown). At the high MOI, icSARS-CoV and icSARS-CoV ΔORF6 genome and subgenomic RNA transcript levels were detected by 6 h postinfection and remained at nearly identical levels at early and late times postinfection (Fig. 1C). In wild-type- but not icSARS-CoV ΔORF6-infected cells, ORF6 protein expression was detected after 24 h and increased through 48 to 54 h postinfection (Fig. 1D). Under identical conditions, membrane glycoprotein expression was detected at 24 h and peaked between 54 and 60 h during both virus infections (Fig. 1E). These results extend previous studies that demonstrated that the SARS-CoV accessory ORF6 interferon antagonist is dispensable at an MOI of >1 (9, 17).

Gene expression analysis in icSARS-CoV- and icSARS-CoV ΔORF6-infected human lung cells. To determine the effect of the removal of ORF6 protein on mRNA synthesis levels and species in SARS-CoV-infected Calu3 2B4 cells, total RNA was harvested in triplicate at the time points described above, and global mRNA expression was analyzed. Little host gene differential expression was detected during the first ~24 h of icSARS-CoV or icSARS-CoV ΔORF6 infection (Fig. 2A to C), supporting previous studies that indicated that coronaviruses enter the host cell "quietly," perhaps by sequestering double-stranded RNA away from or thwarting recognition by the host cell sensing machinery early after infection (56, 57). Overall, a total of 6,947 genes were differentially expressed ($P < 0.05$; 2-fold change) when icSARS-CoV ΔORF6 and icSARS-CoV samples were directly compared across each time point. Figure 2A shows patterns of gene expression after hierarchical clustering with expression values. Most genes were more highly up- or downregulated in icSARS-CoV ΔORF6-infected than in icSARS-CoV-infected cells compared to the mock-infected samples, such that the primary difference between infections was the magnitude of response. This response differential between the two viruses was also apparent when we compared the total number of differentially expressed genes over time for each virus (Fig. 2B). Differential gene expression changes peaked between 48 and 72 h postinfection for both icSARS-CoV and icSARS-CoV ΔORF6. During this time period, significantly more differentially expressed genes were transcribed in icSARS-CoV ΔORF6-infected Calu3 2B4 cells than in icSARS-CoV-infected cells ($P < 0.0001$, chi-square test), likely due to one of the functions described for the ORF6 protein as a transcriptional block, mediated by the prevention of karyopherin nuclear translocation (Fig. 1A and 2B). After 48 h, there was 50 to 80% overlap in differentially expressed genes between time points, suggesting that the pool of differentially expressed genes is relatively consistent later in the time course of infection (Fig. 2C). This pattern of expression, which is also reflected in Fig. 2A, is likely a consequence of the differences in upstream gene regulation between icSARS-CoV ΔORF6 and icSARS-CoV and indicates that early transcriptional regulation by the ORF6 protein results in dramatic changes in host gene expression that are maintained throughout the 72-h time course.

In addition, we noted a trend for delay in the host response to icSARS-CoV ΔORF6 infection, such that icSARS-CoV had more differentially expressed genes early in the time course between 0 and 36 h postinfection (Fig. 2B). Many of the 202 differentially expressed genes between icSARS-CoV ΔORF6 and icSARS-CoV at 0 to 24 h (Fig. 2C) were expressed at similar levels at later time points, indicating that the host response eventually "catches up" for icSARS-CoV ΔORF6. However, some of the most highly differentially expressed genes between the viruses were detected as early as 24 h postinfection, including matrix metalloproteinase 19 (Mmp19), calcitonin α (Calcα), and calcitonin beta (Calcβ). This early response period included genes enriched for interferon signaling and innate immune response pathways, specifically the Jak-STAT, Th17, and interleukin-4 signaling pathways, suggesting that the presence or absence of the ORF6 gene may either mediate early differences in the kinetics of nuclear import or promote an early replication-enhancing phenotype (87). As the latter phenotype was not evident at a high multiplicity of infection (Fig. 1B and C), the former possibility may be more likely.

Enrichment of biological processes following infection. Although previous studies have indicated that the ORF6 protein is an interferon antagonist, it is less clear whether the block in nuclear import specifically targets interferon signaling or represents an outcome associated with a more global block in the import of nuclear cargo, including transcription factors (17). A summary of our overall modeling approach with details of the individual steps is described in Section S3 of the supplemental material and is outlined in Fig. S2 of the supplemental material. To determine the significant biological processes associated with icSARS-CoV ΔORF6 differential gene expression, the data set was first reduced to six clusters by K-means based on common patterns of expression across genes (Fig. 2A), and then significant enrichment ($P < 0.05$) of biological process Gene Ontology categories was calculated for each cluster individually (Fig. 2A). Processes related to

icSARS-CoV ΔORF6 (MOI of 5). Medium from each well was collected and analyzed by plaque assay for viral growth kinetics in Vero E6 cells, while the cells were harvested for either total RNA for transcriptomic or total protein for proteomic analysis. In panel B, data are shown as the average titer obtained at each time point (6 samples per time point) and were plotted as the PFU/ml. Peak titers for both viruses were detected at 36 h postinfection, and no significant differences in viral titers were detected at any time point. Error bars are the standard deviations of the replicate wells. In panel C, total RNA from infected samples was analyzed by real-time PCR to determine the levels of viral mRNA species (genomic RNA, spike subgenomic RNA, and envelope subgenomic RNA) produced over the time course of infection. No significant differences were detected at any time postinfection at a high MOI in human lung epithelial cells. Symbols in panel B: closed circles with unbroken line, icSARS-CoV; closed triangles with dashed line, icSARS-CoV ΔORF6. Color coding for panel C: green bars, icSARS-CoV genomic RNA; orange, icSARS-CoV spike subgenomic RNA; blue bars, icSARS-CoV envelope subgenomic RNA; white bars, icSARS-CoV ΔORF6 genomic RNA; black bars, icSARS-CoV ΔORF6 spike subgenomic RNA; yellow bars, icSARS-CoV ΔORF6 envelope subgenomic RNA. (D and E) Comparison of viral structural protein (M membrane in panel D) and viral accessory protein (ORF6 in panel E) abundance as determined by global proteomics analysis. Values for proteins represent mean protein abundance levels as measured by mass spectrometry. By 24 h postinfection, M protein was detected for each virus, and the amounts increased through 54 h postinfection. The ORF6 protein was detectable exclusively in the icSARS-CoV-infected samples and also increased in expression through 54 h postinfection. Error bars represent standard errors of the means based on mean protein abundance values derived from mass spectrometry readings of three independent samples at each time point. Symbols and abbreviations in panels D and E: blue lines, icSARS-CoV-infected cells; red lines, icSARS-CoV ΔORF6-infected cells; black lines, mock-infected cells.

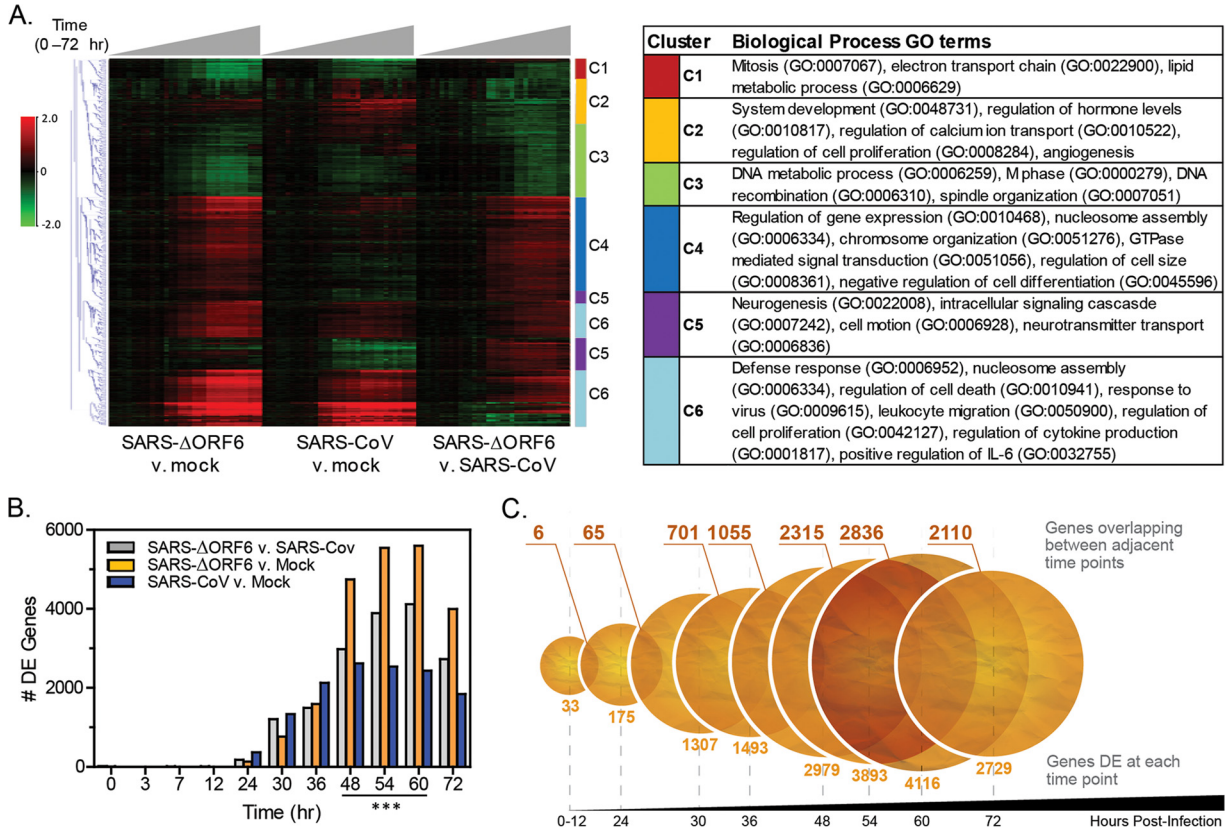

Cluster	Biological Process GO terms
C1	Mitosis (GO:0007067), electron transport chain (GO:0022900), lipid metabolic process (GO:0006629)
C2	System development (GO:0048731), regulation of hormone levels (GO:0010817), regulation of calcium ion transport (GO:0010522), regulation of cell proliferation (GO:0008284), angiogenesis
C3	DNA metabolic process (GO:0006259), M phase (GO:0000279), DNA recombination (GO:0006310), spindle organization (GO:0007051)
C4	Regulation of gene expression (GO:0010468), nucleosome assembly (GO:0006334), chromosome organization (GO:0051276), GTPase mediated signal transduction (GO:0051056), regulation of cell size (GO:0008361), negative regulation of cell differentiation (GO:0045596)
C5	Neurogenesis (GO:0022008), intracellular signaling cascasde (GO:0007242), cell motion (GO:0006928), neurotransmitter transport (GO:0006836)
C6	Defense response (GO:0006952), nucleosome assembly (GO:0006334), regulation of cell death (GO:0010941), response to virus (GO:0009615), leukocyte migration (GO:0050900), regulation of cell proliferation (GO:0042127), regulation of cytokine production (GO:0001817), positive regulation of IL-6 (GO:0032755)

FIG 2 Differentially expressed (DE) genes in icSARS-CoV-infected versus icSARS-CoV ΔORF6-infected Calu3 2B4 cells. (A) Heat map and table of gene ontology categories. The heat map represents unsupervised hierarchical clustering of the 6,947 differentially expressed genes ($P < 0.05$; 2-fold change) between icSARS-CoV and icSARS-CoV ΔORF6 infection of Calu3 2B4 cells, from 0 to 72 h postinfection. Values are the fold change ($\log_2$) compared to time-matched mock infection or icSARS-CoV infection as indicated. Colored bars represent gene tree subclusters. On the right, functional enrichment of significant ($P < 0.05$) biological process Gene Ontology categories for gene tree clusters C1 to C6. Genes within each cluster are indicated on the far right of the heat map. (B) Bar graph of differentially expressed genes ($P < 0.05$, |1.5-fold change| [$\log_2$]) for time-matched comparisons in icSARS-CoV versus mock, icSARS-CoV ΔORF6 versus mock, or icSARS-CoV ΔORF6 versus icSARS-CoV at 0 to 72 h postinfection. ***, from 48 to 72 h postinfection, nearly twice the number of genes were differentially expressed in icSARS-CoV ΔORF6-infected versus icSARS-CoV-infected cells ($P < 0.001$), indicating the ORF6-dependent nuclear import block has been released. (C) Circle diagram of differentially expressed genes between icSARS-CoV ΔORF6 and icSARS-CoV across the time course.

transcription, nuclear signaling, cell proliferation and death, and host antiviral and the immune response were upregulated in icSARS-CoV ΔORF6 compared to icSARS-CoV (clusters C4, C5, and C6), while cell cycle and select metabolic processes, like DNA and lipid metabolism, were downregulated (clusters C1, C2, and C3) (Fig. 2A). These data suggest that the ORF6 protein antagonizes nuclear import processes and host transcription.

Transcription factor analysis. Viral antagonists of nuclear import have been well documented (10–14); however, it is not clear whether these antagonists selectively and/or differentially regulate nuclear cargo importation, resulting in hierarchical and cell-type-specific patterns of antagonism of host gene expression. The SARS-CoV model is particularly appropriate to address this question, as the ORF6 protein binds karyopherin α2, suggesting a selective targeting of cargo. However, the process is further complicated by the ORF6 protein-karyopherin α2 complex's capacity to also sequester karyopherin β1, which is essential for all nuclear import via karyopherins (Fig. 1A). The pattern of expression in gene cluster C4, which included 1,674 genes exclusively upregulated in icSARS-CoV ΔORF6 but unchanged in icSARS-CoV, was enriched in biological processes for chromosome organization and regulation of gene expression and nucleosome assembly. This was particularly interesting, given that one of the ORF6 protein mechanisms of action is prevention of nuclear translocation of karyopherin-dependent cellular factors. Therefore, we focused on the genes in cluster C4 to identify potential downstream targets of karyopherins whose transcription is blocked in icSARS-CoV infection. In particular, we evaluated whether transcription factors whose transport is regulated by karyopherins were overconnected (transcription factors with a significant number of downstream target genes that were differentially expressed, in this case either up- or downregulated [$P < 0.05$]) to downstream gene expression networks (or to downstream genes whose expression is regulated by the same transcription factor) by hypergeometric distribution within the C4 cluster. When the number of connections between target genes in the data set and upstream regulatory transcription factors are greater than would be expected by chance (based on the number of known connections), this indicates that these transcription factors are enriched and are important regulators of the host response by the ORF6 protein. All of the transcription factor hubs (schematically represented by large circles in Fig. 3) associated with gene cluster C4 that were identified as being regulated by karyopherins in MetaCore are listed in Table 1. Six of these transcription factors (VDR, CREB1, Oct3/4, HIFα2/Epas1, p53, and

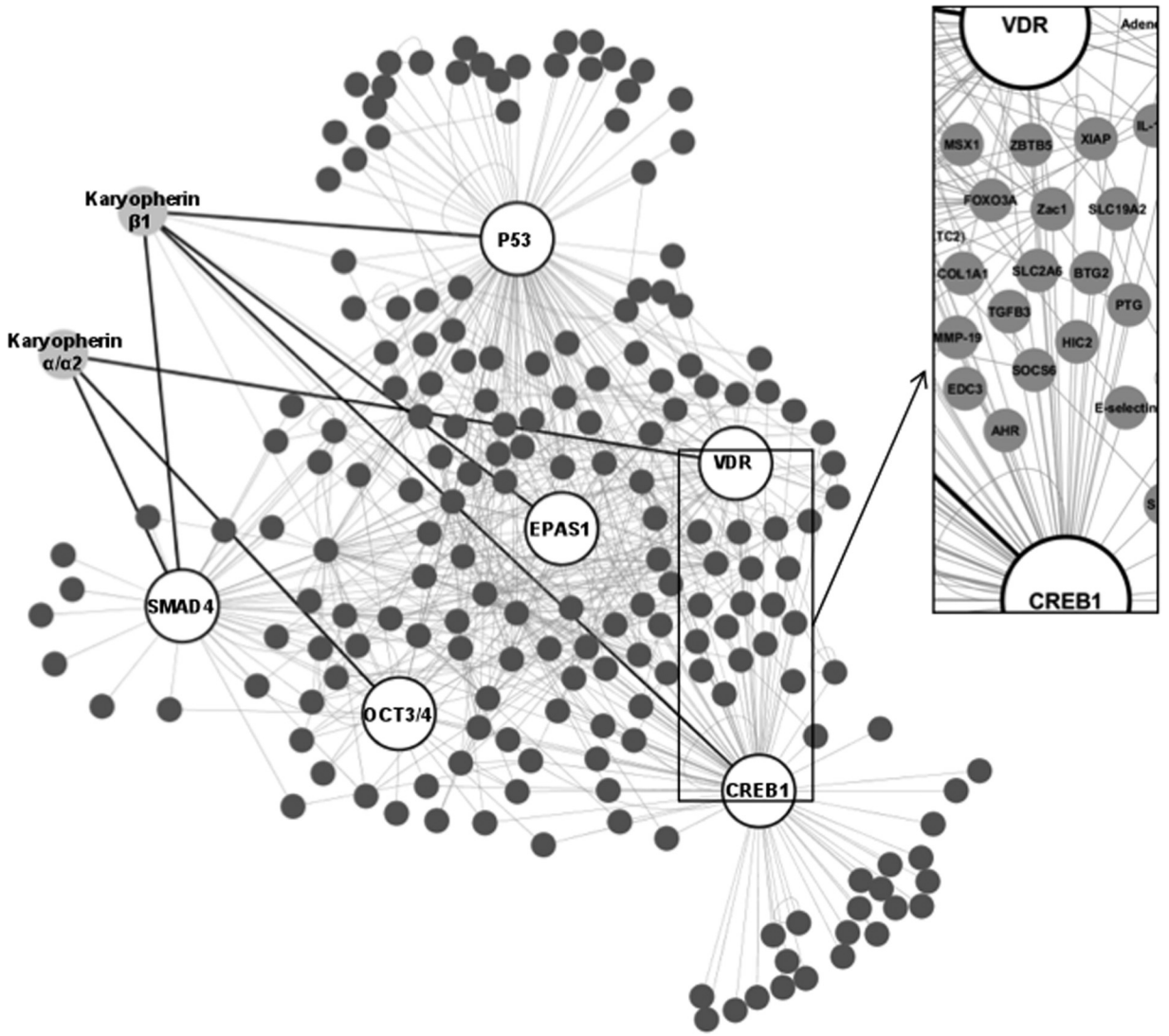

FIG 3 Identification of transcription factor hubs directly affected by removal of ORF6-dependent nuclear import block. The schematic shows the network for significantly overconnected transcription factors ($P < 0.05$) whose nuclear transport is prevented by ORF6 in wild-type SARS-CoV infection. White circles represent overconnected transcriptional hubs; dark gray circles represent target nodes whose relative expression was lower with icSARS-CoV than with icSARS-ΔORF6; light gray circles represent karyopherins; gray lines represent edge connections between hubs, nodes, and karyopherins; heavy black lines represent direct edge connections between karyopherins and transcriptional factor hubs. The enlarged inset includes genes in the VDR and CREB1 networks for which transcriptional patterns were confirmed by HAE transcriptomic and Calu3 2B4 proteomic data (see Fig. 5 and 6, respectively).

SMAD4) were significantly ($P < 0.05$) overconnected to the data set (Table 1), indicating that there was differential signaling through these transcription factor hubs when comparing icSARS-CoV ΔORF6 to icSARS-CoV. Over 350 gene nodes in the C4 cluster directly interact with these six transcription factors (Fig. 3), based on information in the Metacore knowledge base, suggesting their transcription is specifically blocked in the presence of functional ORF6 protein. As a summary of our network analysis, we graphed the fold change over mock for all of the genes regulated by each of the six transcription factors identified by our modeling approaches (Fig. 4A). In each graph, the differentially expressed networks in the icSARS-CoV ΔORF6-infected cells are significantly upregulated (7- to 22-fold increase over mock, which was significant from 48 to 60 h postinfection for all of the transcription factors) compared to steady levels in the icSARS-CoV-infected cells, suggesting that the release of the ORF6 protein-mediated nuclear importation block does affect cellular transcription and is not limited to immune-responsive transcription factors. In contrast, two transcription factors (beta-catenin and androgen receptor) that do not require karyopherin to translocate to the nucleus are shown in Fig. 4B and demonstrate similar differential expression patterns between icSARS-CoV ΔORF6 and wild-type virus (only a 1.5-fold difference above mock, and the changes were significant only at 72 h postinfection for beta-catenin) through 60 h.

The initial targeted approach that identified the six transcription factors was restricted to the subset of genes in cluster C4 (Fig. 2A), which were upregulated exclusively in icSARS-ΔORF6-infected cells. However, we wondered if additional karyopherin-regulated transcription factors were also present in networks generated from the original 6,947 genes (in all 6 clusters) identified

TABLE 1 Transcription factor hubs associated with gene cluster C4[a]

KPNB/B1[b]	KPNA2[c]	Other KPNA[d]
Ap-1	C-myc	Ahr*
C-fos*	**Epas1***	Brca1
C-jun*	Hif1a*	**Epas1***
CREB1*	Iref1	Notch1
Epas1*	Lef1	Nf-κb
Hif1a*	**Oct-3/4***	STAT1
Nf-at1*	Pxr	Stat3*
Nrf2	**SMAD4***	**VDR***
P53*		Zac1
Rxra		
SMAD3*		
SMAD4*		
Snail1*		

[a] *, the transcription factor is overrepresented in the data set, based on the connectivity ratio (actual/expected), calculated as the ratio of the actual number of connections to genes in the C4 cluster (see Fig. 2B) versus the number of connections expected using the Agilent platform. Bold highlighted transcription factors are significantly ($P < 0.05$) overrepresented in the data set.
[b] Karyopherin β (importin β1).
[c] Karyopherin α2 (importin α1).
[d] The "Other KPNA" (karyopherins) category includes karyopherin α1 (importin α5) and karyopherin α3 (importin α4). EPAS1 (HIF2A) uses importins α1, 3, 5, and 7. VDR uses importin α4.

(Fig. 2A), which would suggest that karyopherins import transcription factors that both positively and negatively regulate downstream target genes during the course of SARS-CoV infection. To answer this question, we expanded our transcription factor analysis to include all significant genes in the data set, resulting in 27 overconnected transcription factors whose nuclear importation was mediated by karyopherins (Table 2). This analysis provided a more global understanding of the potential impact of the nuclear importation block during SARS-CoV infection compared to the more targeted approach illustrated in Fig. 3 and 4. For example, STAT1 was identified as an important karyopherin-mediated regulator of gene expression during infection. Our laboratory and others have previously observed nuclear translocation of STAT1 in the absence of the ORF6 protein and the upregulation of common targets (i.e., cyclooxygenase 1 and 2/prostaglandin G/H synthase 1 and 2) in icSARS-ΔORF6-infected but not in wild-type-infected cells (see Fig. S3A and B in the supplemental material) (17, 58). For Calu3 2B4 cells, our data suggest that one of the functions of the ORF6 protein is to mediate complex hierarchical antagonism phenotypes of the nuclear import machinery, antagonizing different cellular responses during virus infection.

Validation of transcription factor hubs in human primary airway epithelial cells. To independently confirm the transcription factors identified from network-based modeling analysis of the microarray data with Calu3 2B4 cells, similar modeling approaches were performed to identify transcription factors from microarray data for icSARS-CoV- and icSARS-CoV ΔORF6-infected primary HAE cell cultures. Total RNA was harvested and analyzed by using an Agilent microarray from wild-type- and icSARS-CoV ΔORF6-infected HAE cultures at multiple times postinfection, and the data were compared to Calu3 2B4 transcriptomic data sets to determine if similar targets (genes downstream of the transcription factors identified from just the Calu3 2B4 microarray data) could be identified in both primary and traditional cell isolates. We first examined the viral growth kinetics in HAE cultures and determined that icSARS-CoV titers peaked at 48 h postinfection (Fig. 5A). In contrast, replication titers for icSARS-CoV ΔORF6 increased over the entire 72-h time course (Fig. 5A). At a slightly reduced MOI (Calu3 2B4 cells at an MOI of 5 versus HAE at an MOI of 2), icSARS-CoV ΔORF6 demonstrated slower growth kinetics until later in infection in primary cells, consistent with a role in early replication (Fig. 5A) and (59). Transcription factor analysis of the HAE data set resulted in 7 enriched transcription factor hubs regulated by karyopherins ($P < 0.05$), including RelA, C-jun, CREB1, Hif1α, C-fos, VDR, and SMAD3. Two of the enriched transcription factor hubs in HAE cultures, CREB1 and VDR, were also identified as important in the targeted Calu3 2B4 analysis of exclusively upregulated differentially expressed genes (cluster C4), whose transcription factors enter the nucleus in a karyopherin-mediated process (Table 1; Fig. 3 and 4), while the other 4 transcription factors overlapped the hubs identified from the global Calu3 2B4 gene microarray data set (Table 2), independently confirming the overlap of target genes regulated by the VDR and CREB1 transcription factors between HAE and Calu3 2B4 cells. A comparison of the CREB1 and VDR transcription factor networks, which were significantly enriched in both HAE and Calu3 2B4 cells, is shown in Fig. 5B (see also Fig. S4 in the supplemental material) and illustrates the genes that are either uniquely regulated by the overconnected transcription factor gene targets in each cell type or are genes that are common to both cell types. The mRNA expression levels (from the microarray data) for representative individual genes that were differentially expressed in both the HAE and Calu3 2B4 microarray data sets are graphed in Fig. 5C for comparison, including the genes B cell translocation gene 2 (Btg2), forkhead box 03a (Foxo3a), hypermethylated in cancer 2 (Hic2), human p-thromboglobulin gene (Ptg), thiamine transporter gene (Scl19a2), glucose transporter gene (Scl2a6), transforming growth factor β3 (TGFβ3), and POK family transcription factor (Zbtb5). Transcription factor analysis in HAE cultures resulted in strong overlap with the transcription factor hubs identified in Calu3 2B4 cells and further supported the importance of karyopherin-mediated nuclear importation during SARS-CoV infection.

Proteomic and ChIP-PCR validation of transcriptional hubs. To independently validate our transcriptomic results, we performed shotgun proteomics using the AMT tag approach and ChIP-PCR, with parallel sets of Calu3 2B4 cells infected with icSARS-CoV and icSARS-CoV ΔORF6. Following proteomic analysis, a total of 864 proteins were significantly ($P < 0.05$) differentially expressed between icSARS-CoV- and icSARS-CoV ΔORF6-infected Calu3 2B4 cells across all time points. To most directly determine how the proteomics contributes to our understanding of the role(s) for the ORF6 protein in karyopherin-mediated nuclear translocation and host gene expression, we first integrated the transcriptomic and proteomic data sets. From the integrated data, we obtained a more comprehensive view of the changes mediated by the ORF6 protein in Calu3 2B4 cells at both the gene and protein levels, allowing us to determine whether karyopherin-mediated transcriptional hubs are further enriched (i.e., more significant) with the addition of the proteomic data. For example, if the proteomic data support a role for the ORF6 protein in karyopherin-mediated nuclear transport, then we would expect an increase in the enrichment scores (increased significance) of these hubs after addition of the proteomics; otherwise, the values would decrease. From a biological perspective, the

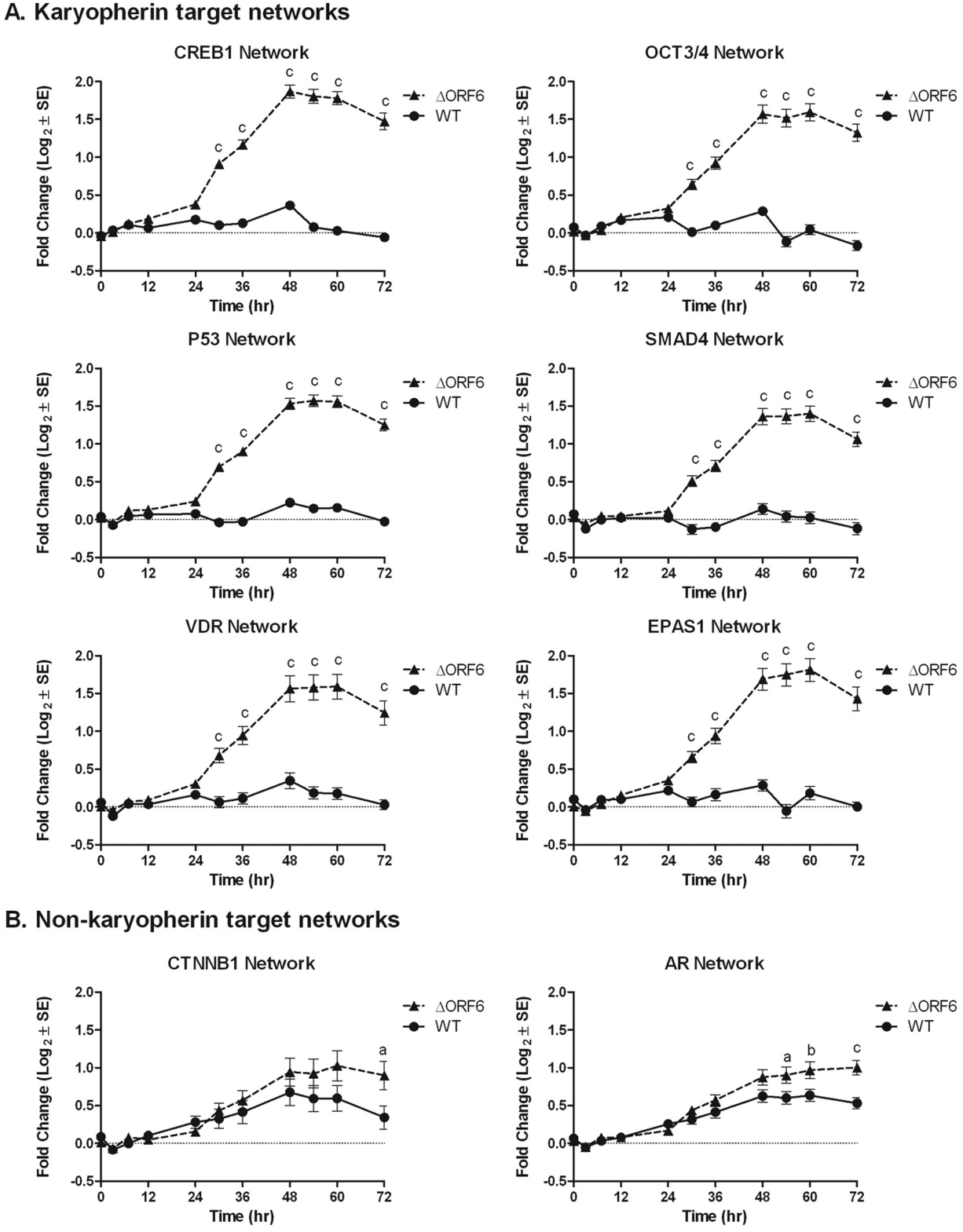

FIG 4 Differential gene expression quantitation for transcription factor networks. Average gene expression for icSARS-ΔORF6 (dotted lines) and icSARS-CoV (solid lines) for target gene nodes (mRNA microarray values for genes regulated by transcription factors) are shown. For each network, a group of genes is regulated by a specific transcription factor. (A) Karyopherin target networks (VDR, CREB1, Oct3/4, p53, EpasI, and SMAD4) from cluster C4 (Fig. 2). (B) Representative nonkaryopherin target network. Values are the average fold change ($\log_2$) ± the standard error compared to time-matched mock infection for 0 to 72 h postinfection. Significant differences in gene expression between icSARS-CoV and icSARS-ΔORF6 at each time point were calculated by a two-way analysis of variance with Bonferroni multiple testing correction and are indicated by the following lowercase letters: a, $P < 0.05$; b, $P < 0.01$; c, $P < 0.0001$. CTNNB1, beta catenin 1; AR, androgen receptor.

TABLE 2 Significantly enriched transcription factor hubs regulated by karyopherins for differentially expressed genes of SARS-CoV versus SARS-ΔORF6

Transcription factor[a]	Calu3 2B4 transcriptomics results[b]				Calu3 2B4 transcriptomics and proteomics *P* value[c,g]
	Actual[d]	Expected[e]	Ratio[f]	*P* value[g]	
p53	450	339.30	1.33	1.92E−12	3.74E−14*
CREB1	364	265.40	1.37	2.79E−12	6.93E−13*
VDR	103	74.82	1.38	1.76E−04	2.13E−05*
Epas1	54	36.94	1.46	1.29E−03	3.78E−05*
SMAD4	121	91.28	1.33	2.95E−04	1.13E−04*
Oct-3/4	156	121.20	1.29	2.09E−04	2.33E−04
C-myc	542	476.90	1.14	1.87E−04	8.21E−17**
Rela	260	182.30	1.43	6.12E−11	9.00E−15**
C-jun	287	197.90	1.45	6.32E−13	1.59E−14*
Sp1	702	595.90	1.18	6.82E−08	2.66E−14**
Hif1a	177	124.90	1.42	1.22E−07	1.46E−10*
Ahr	132	88.93	1.48	2.84E−07	6.88E−09*
Irf1	102	63.52	1.61	9.09E−08	1.06E−08*
GCR-α	199	150.60	1.32	4.94E−06	1.73E−08*
C-fos	155	109.60	1.41	8.49E−07	5.32E−08*
STAT1	164	128.50	1.28	2.29E−04	9.82E−08**
Stat5a	62	36.70	1.69	4.37E−06	6.31E−07*
Relb	52	31.76	1.64	6.71E−05	8.17E−07*
Nf-κb	34	17.17	1.98	1.31E−05	2.64E−05
Irf5	25	11.76	2.13	4.11E−05	7.84E−05
Nfya	49	28.23	1.74	1.82E−05	7.96E−05
Arnt	47	33.41	1.41	5.89E−03	4.84E−04*
Nrf2	76	59.52	1.28	9.82E−03	1.01E−03*
Gata-3	101	79.76	1.27	4.36E−03	3.37E−03*
PPAR-α	61	46.11	1.32	8.78E−03	3.57E−03*
Sox9	54	39.29	1.37	5.73E−03	1.23E−02
SMAD3	152	112.20	1.35	1.56E−05	

[a] Transcription factor hubs regulated by karyopherins and identified as significantly overconnected to data set ($P < 0.05$; 5% FDR). Bold highlighted transcription factor hubs are significant for cluster C4 (see Fig. 2B) and are listed at the top. Otherwise, transcription factors were ranked based on the *P* value for transcriptomics and proteomics.

[b] Values for differentially expressed genes in the SARS-CoV versus SARS-ΔORF6 Calu3 2B4 transcriptomics data set (6,947 genes), using the Agilent platform data as background.

[c] Values for differentially expressed genes and proteins in SARS-CoV versus SARS-ΔORF6 Calu3 2B4 transcriptomics and proteomics data sets combined (6,947 genes, 871 proteins). *, *P* values were more significant than for transcriptomics alone; **, *P* values were >1,000-fold greater than for transcriptomics alone.

[d] Number of genes in the experimental data set that interacted with the transcription factor.

[e] Number of genes in the experimental data set predicted to interact with the transcription factor based on the total number of interactions on the Agilent platform and calculated as the mean value for the hypergeometric distribution.

[f] Connectivity ratio (actual/expected).

[g] Probability for a given value of the actual value or higher (FDR-adjusted $P < 0.05$).

enrichment scores (*P* values) represent how connected the transcription factors are to downstream targets (genes or proteins) in the data set compared to the number of targets expected by chance. If a transcriptional hub is significantly ($P < 0.05$) more connected to the data set, this suggests that signaling through this hub is uniquely regulated, based on the experimental conditions: in this case, through deletion of ORF6. We can use the integrated gene and protein data to identify significant hubs whose downstream targets may primarily be detected at the protein level and whose enrichment scores are greatly elevated by inclusion of the proteomics data. In our study, transcription factor analysis of the combined Calu3 2B4 proteomics and transcriptomics data resulted in an increase in enrichment scores, ranging from 1.5×10^{12}- to 2×10^{12}-fold, for 22 out of 27 of the transcription factor hubs requiring karyopherin for nuclear importation, including 5 out of the 6 transcription factor hubs uniquely upregulated during icSARS-CoV ΔORF6 infection (Table 2). This suggests that many protein nodes in the proteomic data set share common upstream transcription factor regulators with gene nodes in the transcriptional data, including those that require karyopherin for nuclear import. For four transcription factor hubs in particular, C-myc, Rela, specificity protein 1 (Sp1), and STAT1, values from the combined transcriptomic/proteomic analysis were >1,000-fold more significant than for the transcriptomics alone, demonstrating the added value of including targets from both data types (Table 2). In support of the transcription factor analysis, expression levels of individual downstream targets were confirmed between Calu3 2B4 transcriptional and proteomics analyses. Enhancer of mRNA-decapping enzyme 3 (EDC3) and Golgi apparatus adapter-related complex of proteins mu 1 subunit (AP3M1), two target gene nodes predicted to be a part of CREB1 networks, were measured at both the transcript and protein levels (Fig. 6). Individual RNA expression values derived from microarray analysis demonstrated increased RNA expression trends in icSARS-CoV ΔORF6 versus icSARS-CoV in both EDC3 and AP3M1 (Fig. 6A and C). Coordinately, protein abundance also increased at late times during icSARS-CoV ΔORF6 infection; in contrast, icSARS-CoV infection protein levels failed to rise above mock infection values (Fig. 6B and D). When directly compared, both gene and protein analyses demonstrated augmentation of these gene nodes in icSARS-CoV ΔORF6 infection at late times compared to icSARS-CoV infection. Together, these data confirm increased expression of targeted gene nodes downstream of identified transcriptional factors in icSARS-CoV ΔORF6 infection, increases that are absent in icSARS-CoV infection.

Finally, to demonstrate that the transcription factors we identified were actively engaged in transcription during icSARS-CoV ΔORF6 infection, we performed ChIP followed by real-time PCR (ChIP–RT-PCR) of target gene transcripts. Calu3 2B4 cells were infected with icSARS-CoV or icSARS-CoV ΔORF6 or mock infected, protein and DNA were cross-linked, genomic DNA was sheared, and VDR- and CREB1-bound DNA promoter regions were precipitated with antisera directed against each of these transcription factors. Next, gene-specific primer pairs were used to amplify DNA regions of interest by real-time PCR. The results for transcription factor-specific antisera were compared to control IgG precipitations and time-matched mock-infected controls. We chose to amplify three representative downstream target genes: the matrix metalloproteinase 19 (MMP19) and cyclin-dependent kinase inhibitor 1A (CDKN1A) CREB1-regulated genes, as well as the myeloid leukemia cell differentiation gene (Mcl-1), a downstream target of VDR. Figure 7 shows the significant increase in the amount of chromatin precipitated relative to the fold enrichment in icSARS-CoV ΔORF6-infected samples for MMP19, CDKN1A, and Mcl-1 at both 24 and 48 h postinfection compared to wild-type icSARS-CoV. These results confirm that at least two transcription factors identified by modeling are significantly enriched on the promoter elements of their target genes following icSARS-CoV ΔORF6 infection, supporting the microarray data and validating our modeling approaches.

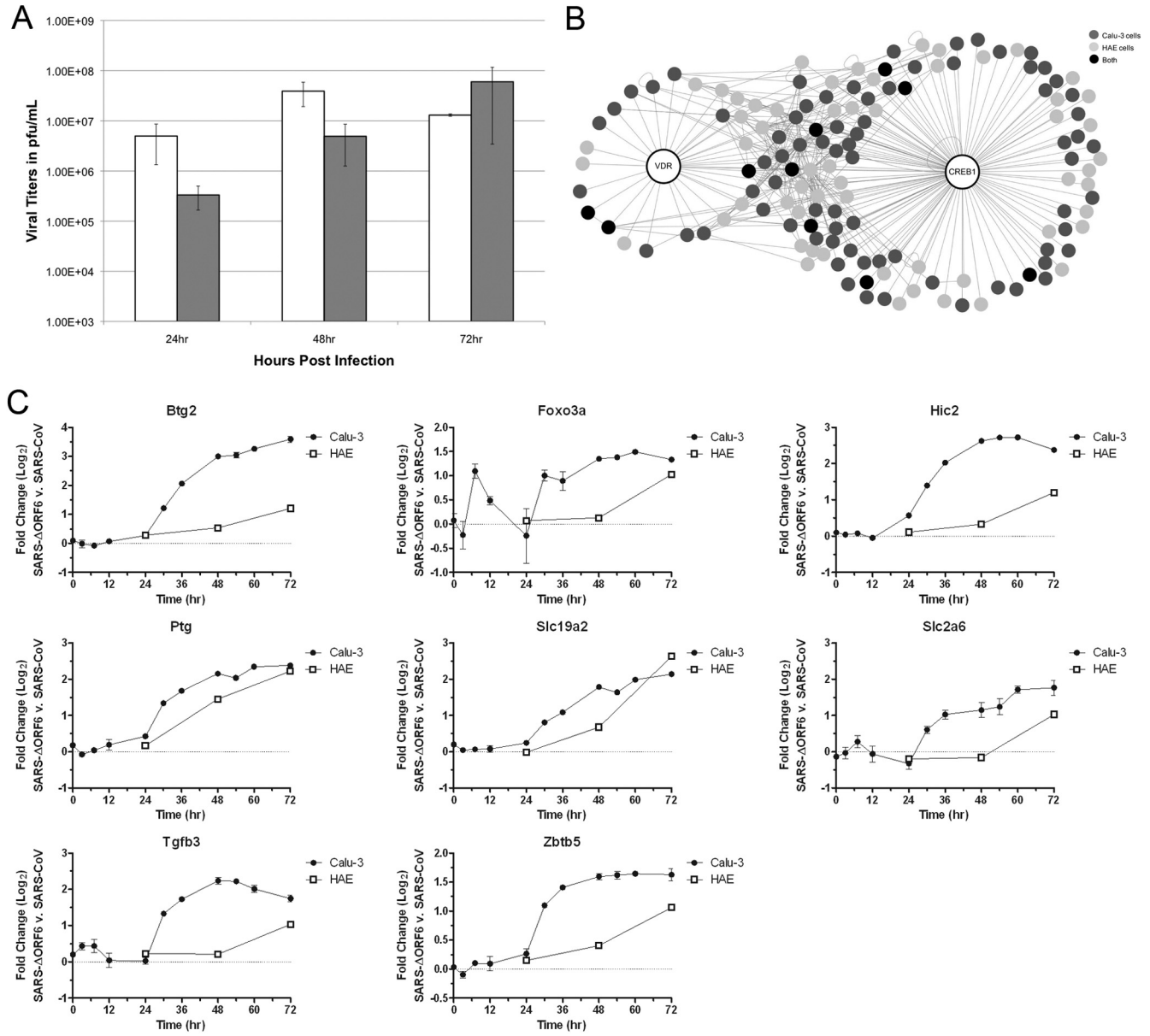

FIG 5 HAE independent confirmation studies. HAE cells were infected with wild-type or SARS-CoV ΔORF6 (MOI of 2) and harvested at 24, 48, and 72 h postinfection for microarray analysis. (A) Apical wash samples were collected in triplicate at the indicated times and assessed by plaque assay in Vero E6 cells. Data are the average titers obtained at each time point (3 samples per time point) and were plotted as PFU/ml. icSARS-CoV titers (white bars) increased through 48 h postinfection and then decreased slightly at 72 h postinfection. In contrast, replication titers for icSARS-CoV ΔORF6 titers (gray bars) increased over the entire course of the infection. At a slightly reduced MOI (Calu3 2B4 cell MOI of 5, versus HAE MOI of 2), icSARS-CoV ΔORF6 demonstrated slower growth kinetics until later in infection in primary cells. (B) Karyopherin-mediated VDR and CREB1 transcription factor networks were significantly ($P < 0.05$) enriched for both Calu3 2B4 and HAE data sets. Light gray circles, gene nodes from the Calu3 2B4 experiment; dark gray circles, gene nodes from the HAE experiment; black circles, gene nodes that overlapped in the two experiments. (C) Comparison of gene expression in Calu3 2B4 cells (closed circles) and HAE cells (open squares) postinfection for target gene nodes downstream, VDR and CREB1. Values are the fold change ($\log_2$) for icSARS-ΔORF6 versus icSARS-CoV. Calu3 2B4 cell results represent the average expression level ± the standard error for 3 replicates on individual arrays. HAE cell results represent the average expression for 2 replicates pooled on arrays. Scl19a2, thiamine transporter gene; Scl2a6, glucose transporter gene; Abtb5, POK family transcription factor.

icSARS-CoV ΔORF6 is attenuated at low MOIs and *in vivo*. Airway epithelial cells are major targets for SARS-CoV infection in humans and in mice (36, 60–62). Functional characterization of the gene sets differentially induced following icSARS-CoV ΔORF6 and icSARS-CoV infection in either traditional human lung cell monolayers or primary HAE cultures revealed significant induction of a number of key antiviral response genes (Fig. 8A) that may play critical roles in the host response or in promoting efficient virus replication. These data are consistent with the possibility that icSARS-CoV ΔORF6 might be less capable of maintaining efficient viral replication under more natural conditions (i.e., at a lower MOI) *in vitro*. For example, low numbers of virus-infected cells early in infection would afford robust antiviral host gene expression and paracrine signaling, potentially limiting secondary

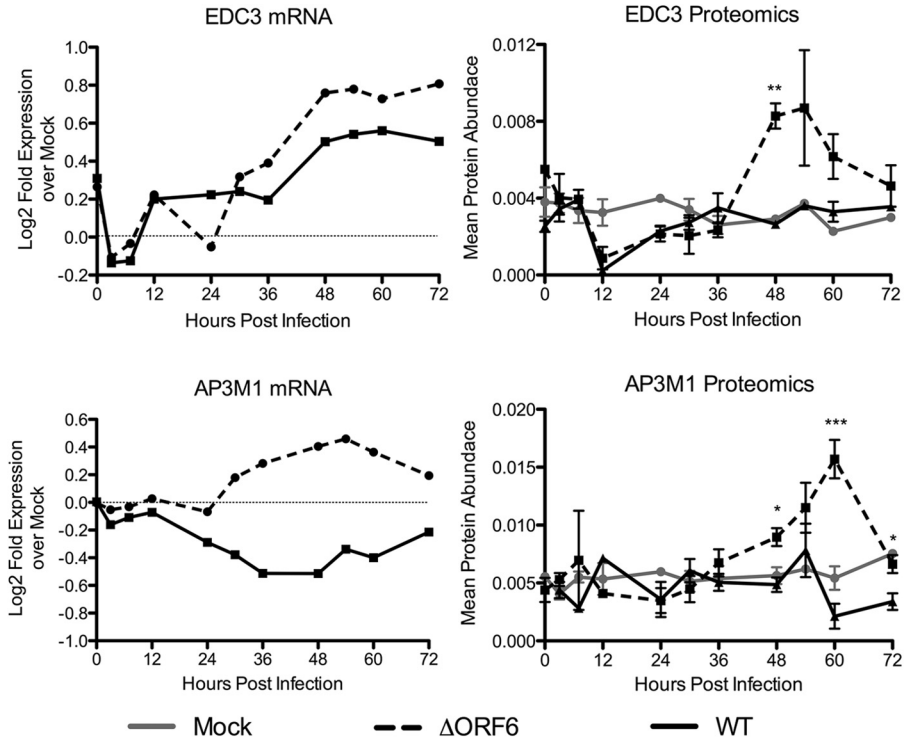

FIG 6 Proteomic validation studies. The graphs show comparisons of individual gene RNA expression (left panels) and protein abundance (right panels) as determined by microarray and global proteomics analysis for EDC3 and AP2M1. Values for transcripts reflect the $\log_2$-fold change in expression over mock infection. For proteins, values represent mean protein abundance levels as measured by mass spectrometry. Error bars represent standard errors of the means based on mean protein abundance values derived from mass spectrometry readings of three independent samples at each time point. EDC3, enhancer of mRNA-decapping protein 3; AP3M1, adaptor-related protein complex 3. Solid gray lines, mock-infected samples; dotted lines, ΔORF6-infected samples; solid black lines, wild-type-infected samples. *P* values were determined with the Student *t* test as indicated. *, $P < 0.05$; **, $P < 0.01$; ***, $P < 0.001$.

rounds of viral replication. To test this hypothesis *in vitro*, we infected Calu3 2B4 cells at a low MOI (MOI of 0.01) with icSARS-CoV or icSARS-CoV ΔORF6 and assessed viral titers by plaque assays in Vero E6 cells. Peak titers for wild-type virus were detected at 72 h postinfection ($\sim 10^7$ PFU/ml), while in contrast, peak titers for icSARS-CoV ΔORF6 ($\sim 10^6$ PFU/ml) were detected at 96 h postinfection and titers were reduced by 1 to 2 logs at all time points examined (Fig. 8B). These data are in contrast to previously published reports (9, 59) in which titers in Vero E6 cells were compared, and the differences can likely be attributed to the intact innate immune and other antiviral signaling pathways present in the human conducting airway Calu3 2B4 cell line. Subsequent studies using another recombinant SARS-CoV that does not express the ORF6 protein have also demonstrated that at a low MOI (MOI of 0.01) in nonhuman primate kidney cells, 2- to 5-fold reductions in viral titers were detected between 6 and 24 h postinfection (77).

To test the hypothesis that the release of the nuclear importation block mediated by the ORF6 protein might attenuate pathogenesis, 20-week-old B6 mice ($n = 5$ mice/time point) were infected with 10^5 PFU of icSARS-CoV mouse-adapted virus or icSARS-CoV ΔORF6 mouse-adapted virus. Weight loss was measured each day, and lungs were harvested to assess viral titers at days 1, 2, 4, and 7 postinfection. Mice infected with icSARS-CoV mouse-adapted virus steadily lost weight over the 7 days of infection, while in contrast, mice infected with icSARS-CoV ΔORF6 mouse-adapted virus lost weight through 4 days postinfection and then began to recover and gain weight (Fig. 8C). Weight loss in animals infected with icSARS-CoV ΔORF6 mouse-adapted virus was significantly different than in mice infected with icSARS-CoV mouse-adapted virus at days 2 to 7 postinfection ($P < 0.01$ by Student's *t* test). Mock-infected mice lost no weight over the course of the infection. Lung titers for both viruses were determined by plaque assay, and no significant differences were measured at days 1, 2, or 7 postinfection. However, at 4 days postinfection, titers in the mouse-adapted icSARS-CoV ΔORF6-infected mice were significantly higher than mouse-adapted icSARS-CoV-infected mice, despite their weight gain, suggesting that viral growth kinetics were uncoupled from pathogenic outcome (Fig. 8D) following the removal of ORF6 protein expression. Future studies will examine the transcriptional and proteomic profiles of the infected mouse lungs, including those of targeted knockout mice, but these studies are beyond the scope of the current work.

DISCUSSION

Viral antagonism of host cellular processes is well recognized as a major mechanism for regulating viral pathogenesis and virulence. SARS-CoV encodes several interferon antagonists that delay host cell recognition of infection, innate immune sensing, and signaling pathways, as well as interferon-stimulated gene expression; one antagonist, ORF6 protein, does so by blocking nuclear import. Many other highly pathogenic RNA viruses encode proteins that specifically antagonize nuclear import to prevent host innate

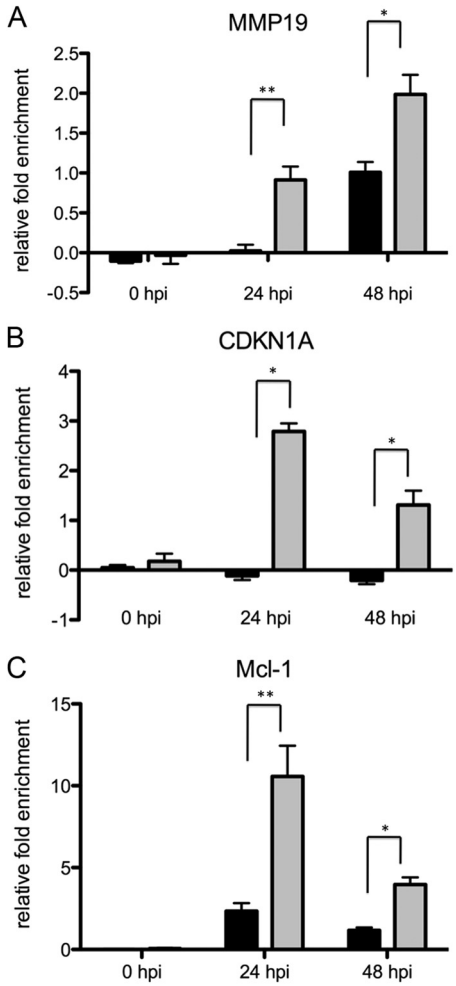

FIG 7 Verification of CREB1 and VDR downstream target genes in icSARS-CoV- and icSARS-CoV ΔORF6-infected Calu3 2B4 cells. Calu3 2B4 cells were infected with icSARS-CoV or icSARS-CoV ΔORF6, or mock infected, and then harvested for ChIP at 0, 24, and 48 h postinfection. ChIP was performed with anti-CREB (MMP19, CDKN1A), anti-VDR (MCL-1), and anti-IgG antibodies (negative control) on each set of samples, and selected target genes whose expression was regulated by either CREB1 or VDR, as identified by microarray analysis, were verified by quantitative real-time PCR. The relative fold enrichment levels for Mcl-1 (a), CDKN1A (b), and MMP19 (c) for icSARS-CoV- or icSARS-CoV ΔORF6-infected Calu3 2B4 cells over the 48-h time course are shown. The C_T values were analyzed by using the standard curve method, and each sample was normalized to the appropriate IgG sample and to the corresponding time-matched mock infection sample. Data are the means ± standard errors of the means for triplicate experiments. *, $P < 0.05$; **, $P < 0.01$ (Student's *t* test). Gray bars, icSARS-CoV ΔORF6; black bars, icSARS-CoV.

immune and other critical cellular macromolecular processes to enhance virus replication and transmission between hosts. For example, Ebola virus VP24 binds karyopherin α1 and blocks STAT1 nuclear import (10). The Nipah virus W protein is localized to the nucleus, where it inhibits both virus- and Toll-like receptor 3-triggered signaling in the infected cell by preventing the phosphorylation and activation of STAT1 and subsequent downstream interferon-stimulated gene induction (11). Some cardiovirus L proteins interact directly with Ran-GTPases, which are required for the export of new nuclear mRNA (12). In these systems, observations were conducted using candidate gene markers, limiting full recognition of the impact of viral antagonism gene function on nuclear translocation during infection. To redress this limitation, we used systems biology approaches that integrated transcriptomic and proteomic data sets in primary and traditional human lung epithelial cells to identify the impact of the ORF6 protein on host macromolecular processes. An advantage of the SARS-CoV ORF6 protein model is that recombinant viruses lacking ORF6 expression are viable and replicate efficiently *in vitro* and *in vivo* (9, 59). Our data support the hypothesis that antagonists of nuclear translocation differentially target host signaling pathways, perhaps in a tissue- and cell-specific manner, to prevent antiviral defenses and other subcellular responses that may limit virus replication. The data reported herein suggest that other viral nuclear import antagonists likely antagonize multiple host transcription factors and cellular processes to allow efficient virus replication, transmission, and spread. Although speculative, these antagonists likely block paracrine signaling of cytoplasmic cargo (e.g., cytokines, steroids, hormones), blocking cellular antiviral responses during virus infection.

Viral antagonists that target nuclear translocation provide a novel model system to study the regulated inhibition of host response networks in the context of virus infection. One of the current ORF6 protein functional paradigms is that it blocks nuclear import by binding karyopherin α2 on internal membranes, sequestering karyopherin β1 and preventing karyopherin-regulated nuclear import of key antiviral transcription factors, like STAT1. However, STAT1 typically uses karyopherin α1 and β1 for import, suggesting that the primary targets for the ORF6 protein may actually be other key host response transcription factors and expression networks during infection. Given the unique biochemical targeting of the ORF6 protein and the fact that SARS-CoV also encodes other proteins that antagonize innate immune signaling (63, 64), it is not surprising that STAT1 was not positioned more prominently as one of the key transcription factors targeted by ORF6 protein antagonism of nuclear import in either Calu3 2B4 and HAE cultures. The global genomics-based technologies used in this study provide an alternative approach to evaluate the role of specific viral genes on host transcription and proteomic regulatory networks during infection. We recognize that karyopherin and cargo concentrations are heavily cell type dependent, and thus the ORF6 protein's effect on nuclear import in other permissive cell types might result in dramatically different hierarchical activities, leading to variations in host gene expression networks and/or the activation of alternate transcription factors (17, 31, 65, 66). Although our initial studies focused on a recombinant virus that lacked the entire ORF6 gene, future studies using recombinant viruses lacking either the N- or C-terminal portion of the ORF6 protein in early virus replication and nuclear import may provide further resolution to the precise domains in the ORF6 protein that mediate these phenotypes.

In support of earlier reports (9, 17, 59), deletion of ORF6 had minimal effects on the efficiency of virus replication in Calu3 2B4 and HAE cultures; however, these growth comparisons were performed at a high MOI, which is often a less powerful barometer of virus growth than studies with a low MOI in culture. The Calu3 2B4 and HAE culture systems represent continuous and primary models of the human airway epithelium, a major target for early SARS-CoV infection and replication *in vivo* in many species (36, 59, 67). Thus, host response outcomes in these cells likely model *in vivo* responses that inform downstream innate and adaptive im-

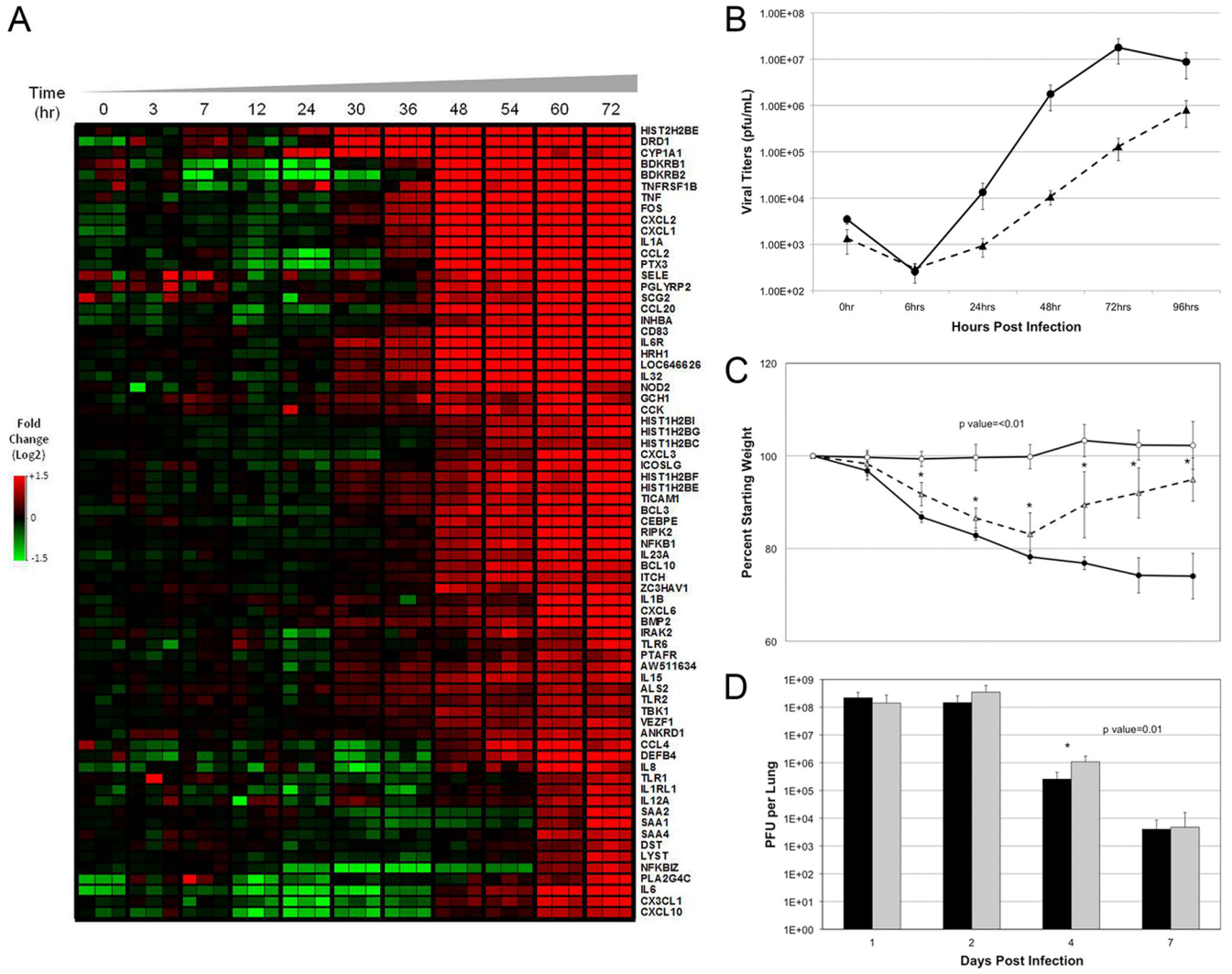

FIG 8 icSARS-CoV ΔORF6 is attenuated at low MOIs and in B6 mice. (A) Gene expression for antiviral pathways. Hierarchical clustering by Euclidean distance of genes from two enriched biological process GO categories from Fig. 2B (cluster C6), the "defense response" (GO:0006952) and "response to virus" (GO: 0009615). A total of 71 out of 96 genes in these pathways were significantly upregulated in icSARS-CoV ΔORF6 compared to icSARS-CoV between 0 and 72 h postinfection in Calu3 2B4 cells and are presented in the heat map. Values are the fold change ($\log_2$) in icSARS-CoV ΔORF6 versus icSARS-CoV at each time point. Red, green, and black represent upregulated, downregulated, and unchanged genes, respectively. (B) Low-MOI Calu3 2B4 cell infection. Calu3 2B4 human lung cells were infected with either icSARS-CoV or icSARS-CoV ΔORF6 (MOI of 0.01). Medium from each well was collected and analyzed by plaque assay for viral growth kinetics in Vero E6 cells. Data are the average titer obtained at each time point (3 samples per time point) and were plotted as PFU/ml. Peak titers for icSARS-CoV were detected at 72 h postinfection, while titers for icSARS-CoV ΔORF6 peaked at 96 h postinfection, suggesting that the mutant was attenuated at a low MOI over the course of the infection. Closed circles and unbroken line, icSARS-CoV; closed triangles and dashed line, icSARS-CoV ΔORF6. (C and D) Weight loss (C) and titer data (D) for 20-week-old B6 mice ($n = 5$) infected intranasally with 10^5 PFU of virus. Weight loss was assessed each day postinfection through day 7, and titers were assessed at the indicated times postinfection. Mice infected with icSARS-CoV mouse-adapted virus steadily lost weight over the course of the infection; in contrast, mice infected with the icSARS-CoV ΔORF6 mouse-adapted virus lost weight until day 4 postinfection, when they began to recover from infection and to gain weight. Mock-infected mice had no appreciable weight loss at any time postinfection. Symbols in panel C: closed circles and solid line, icSARS-CoV mouse-adapted virus; open triangles and dotted line, icSARS-CoV ΔORF6 mouse-adapted virus; open circles and solid line, mock infection. No significant differences in titers were detected at days 1, 2, or 7 days postinfection. Open circles, mock infection; gray triangles, icSARS-CoV ΔORF6 infection; filled circles, icSARS-CoV infection. Error bars indicate standard deviations from the means. Asterisks indicates a P value of <0.01 for icSARS-CoV mouse-adapted virus versus icSARS-CoV ΔORF6 mouse-adapted virus. Box colors in panel D: black, icSARS-CoV; gray, icSARS-CoV ΔORF6.

mune responses during infection. At lower MOIs, more subtle effects of the ORF6 protein have been reported on virus replication rates, especially early, but not late, in infection (59, 68). While our data in HAE and Calu3 2B4 cultures support these earlier findings, we designed the current experiment to include a high MOI to reduce the impact of paracrine signaling between infected and uninfected cells, allowing us to specifically focus on host responses during infection. Importantly, in the presence or absence of the ORF6 protein, similar RNA expression kinetics and levels of virus replication were noted in both Calu3 2B4 cells and HAE cultures; thus, the virus effects on differential gene expression likely reflected the targeted activities of the ORF6 protein directly on virus-host regulated interactions, like nuclear translocation. However, there were dramatic differences in the levels and rates of

differential gene expression detected between the two viruses despite similar replication kinetics. icSARS-CoV differential gene expression was detectable as early as 24 h postinfection and was higher than the levels detected for icSARS-CoV ΔORF6 through 36 h postinfection. At 48 h postinfection, a drastic change occurred with the number of differentially expressed genes still increasing for icSARS-CoV, but the number of genes detected for icSARS-CoV ΔORF6 jumped to twice the level of the wild type (Fig. 2B, ΔORF6 36 h 1600 versus 48 h 4750), a trend which continued through 72 h postinfection. These data tracked with levels of detectable ORF6 protein expression (Fig. 1D) and suggest that the changes mediated by the ORF6 protein during infection can likely be uncoupled from replication kinetics but still modulate pathogenesis, as seen with the weight loss recovery in the mouse model (Fig. 8C and D).

Several of the identified transcription factors play critical roles in lung cancer but can also mediate many acute and chronic lung disease phenotypes. During normal lung development, CREB1 plays an important role in the differentiation of the mucin- or mucus-producing cells (69). In contrast, studies have also demonstrated that CREB1 and its associated pathways contribute to pathological lung disease progression via inflammatory response-mediated lung remodeling postinfection/post-lung injury (70, 71). VDR transcription factor levels are reduced in patients with chronic obstructive pulmonary disease (COPD), and vitamin D has been shown to be important in the onset of COPD (72, 73). In VDR knockout mice, increased lung inflammation and emphysema were noted, suggesting an important role for VDR signaling in normal lung function and lung disease prevention or exacerbation (74). The transcription factor EpasI/HIFα2 is critical for responding to reduced oxygen levels in the intracellular environment (75). EpasI/HIFα2 is part of the hypoxia response and was one of the genes detected in the microarray analysis of wild-type SARS-CoV-infected nonhuman primates, whereas in the presence of the ORF6 protein its expression was downregulated (76, 77). The SMAD family of transcription factors are potent inducers of TGF-β, which can activate apoptosis signaling pathways during influenza virus infection (78). SMAD proteins as well as p53 have also been implicated as being underexpressed in a wide variety of cancers, including lung carcinomas (23, 79). Many viruses have designed strategies to counter p53 signaling (80–83). Importantly, p53 expression enhances innate immunity by enhancing IFN-dependent antiviral activity via IRF-9 activation, independent of its functions as a proapoptotic and tumor suppressor gene (80). In some cell lines, influenza virus infection can increase p53 expression, where it is essential for the induction of cell death phenotypes, and loss of p53 expression enhances virus growth (81). SARS-CoV targets and infects Oct 4-expressing pluripotent lung stem cells, which differentiate into type 1 and type 2 pneumocytes, and is essential for repair and function of the alveoli (84). Lung stem cells are reported targets for SARS-CoV infection, and so blocking Oct 4 expression may well slow the rate of recovery from lung injury by preventing differentiation of stem cells that are essential for normal lung function and wound repair (85). All of the transcription factor hubs identified by modeling of systems biological approaches play critical roles in the regulation and maintenance of lung cell homeostasis and would not have been collectively identified in more-targeted studies.

Enrichment of karyopherin-mediated transcription factors in icSARS-CoV ΔORF6 infection compared to infection with the wild type was independently confirmed and validated from analysis of different data sets, including proteomics and ChIP-PCR data from infected Calu3 2B4 cells and microarray data from infected HAE cultures. It is reassuring that bioinformatic approaches independently validated earlier biochemical studies, demonstrating targeted antagonism of nuclear import by using a candidate gene approach. ChIP-PCR analysis demonstrated that some transcription factors identified by modeling approaches were actively bound to the promoters of specific downstream target genes (identified by microarray analysis), lending further credence to the modeling analysis (55, 86). The strength of the current approach is that global integration of data in the context of biological pathways or functional processes, such as transcriptional factor regulation, provide a complementary interpretation of genomic and proteomic results that is necessary for systems-level comparisons (87). Direct comparison or integration of heterogeneous data sets is complicated by inherent differences among cell types, platforms, and technologies. However, the identification of common regulatory components that induce gene or protein signatures across model platforms can provide important information about underlying biological processes during infection (88). The overlap in regulatory events across systems, including comparison of infection of traditional cell lines to infection of primary human cells, can be considered independent confirmation of the mechanism of action for the ORF6 protein during SARS-CoV infection. In this study, a range of approaches were applied to provide a comprehensive view of karyopherin-dependent nuclear importation mediated by the ORF6 protein during SARS-CoV infection, and these approaches were not only validated across systems but also could be interpreted within the context of *in vitro* and *in vivo* viral endpoints.

Removal of the ORF6 protein-mediated nuclear importation block attenuated SARS-CoV pathogenesis in a 20-week-old B6 mouse model. There was no difference in viral growth kinetics between icSARS-CoV and icSARS-ΔORF6 in human lung cells (Calu3 2B4) at high MOIs, and in the 20-week-old mouse model replication patterns were similar between the two viruses, with significant titer differences at only a single time point. However, despite similar virus loads in the lung, weight loss was significantly reduced in mice infected with icSARS-CoV ΔORF6 mouse-adapted virus compared to those infected with wild-type mouse-adapted virus, suggesting that viral titers do not necessarily correlate with disease outcomes. Similar findings have been noted with recombinant SARS-CoV bearing zoonotic Spike glycoproteins, like HC/SZ/61/03 (77, 89). The category of genes most affected by release of ORF6 protein nuclear importation block *in vitro*-regulated overall gene expression, cellular rearrangement for division, and factors required for differentiation, suggesting that the intracellular environment may play a substantial role in determining levels of viral pathogenesis and controlling the intracellular antiviral state.

Antagonists of nuclear import likely contribute to the virulence of many highly pathogenic viruses. Importantly, some of the transcription factors identified in cell culture models, like STAT1, which is significantly regulated by ORF6 protein function, have also been demonstrated to alter *in vivo* pathogenesis (60). In STAT1 knockout mice, but not IFNR knockout mice, icSARS-CoV mouse-adapted infection resulted in dysregulation of T cell and macrophage differentiation, leading to a Th2-biased immune response and the development of alternatively activated macro-

phages that mediated a lethal, profibrotic environment within the lung (90). Future studies will evaluate icSARS-CoV and icSARS-CoV ΔORF6 pathogenesis in p53, CREB1, EpasI, and VDR knockout mice. In addition to antagonizing innate immune signaling, our data argue that antagonists of nuclear import likely target alternative and perhaps unappreciated host signaling networks to maximize a favorable environment for virus replication and pathogenesis, both *in vitro* and *in vivo*.

ACKNOWLEDGMENTS

We thank the team at the UNC Cystic Fibrosis Center Tissue Culture Core for providing primary cells. We gratefully acknowledge the helpful comments and discussions provided by Lynn Law and Sean Proll and critical reviews of the manuscript by Lisa Lindesmith and Rachel Graham.

This project has been funded in whole or in part with federal funds from the National Institute of Allergy and Infectious Diseases, National Institutes of Health, Department of Health and Human Services, under contract HHSN272200800060C. A portion of the research was performed in the Environmental Molecular Sciences Laboratory, a national scientific user facility sponsored by the Department of Energy (DOE) Office of Biological and Environmental Research and located at Pacific Northwest National Laboratory (PNNL). PNNL is operated by Battelle Memorial Institute for the DOE under contract DE-AC05-76RLO1830.

REFERENCES

1. **Drosten C, Gunther S, Preiser W, van der Werf S, Brodt HR, Becker S, Rabenau H, Panning M, Kolesnikova L, Fouchier RA, Berger A, Burguiere AM, Cinatl J, Eickmann M, Escriou N, Grywna K, Kramme S, Manuguerra JC, Muller S, Rickerts V, Sturmer M, Vieth S, Klenk HD, Osterhaus AD, Schmitz H, Doerr HW.** 2003. Identification of a novel coronavirus in patients with severe acute respiratory syndrome. N. Engl. J. Med. **348**:1967–1976.
2. **Ksiazek TG, Erdman D, Goldsmith CS, Zaki SR, Peret T, Emery S, Tong S, Urbani C, Comer JA, Lim W, Rollin PE, Dowell SF, Ling AE, Humphrey CD, Shieh WJ, Guarner J, Paddock CD, Rota P, Fields B, DeRisi J, Yang JY, Cox N, Hughes JM, LeDuc JW, Bellini WJ, Anderson LJ.** 2003. A novel coronavirus associated with severe acute respiratory syndrome. N. Engl. J. Med. **348**:1953–1966.
3. **Guan Y, Zheng BJ, He YQ, Liu XL, Zhuang ZX, Cheung CL, Luo SW, Li PH, Zhang LJ, Guan YJ, Butt KM, Wong KL, Chan KW, Lim W, Shortridge KF, Yuen KY, Peiris JS, Poon LL.** 2003. Isolation and characterization of viruses related to the SARS coronavirus from animals in southern China. Science **302**:276–278.
4. **Lau SK, Woo PC, Li KS, Huang Y, Tsoi HW, Wong BH, Wong SS, Leung SY, Chan KH, Yuen KY.** 2005. Severe acute respiratory syndrome coronavirus-like virus in Chinese horseshoe bats. Proc. Natl. Acad. Sci. U. S. A. **102**:14040–14045.
5. **Lau SK, Woo PC, Li KS, Huang Y, Wang M, Lam CS, Xu H, Guo R, Chan KH, Zheng BJ, Yuen KY.** 2007. Complete genome sequence of bat coronavirus HKU2 from Chinese horseshoe bats revealed a much smaller spike gene with a different evolutionary lineage from the rest of the genome. Virology **367**:428–439.
6. **Li W, Shi Z, Yu M, Ren W, Smith C, Epstein JH, Wang H, Crameri G, Hu Z, Zhang H, Zhang J, McEachern J, Field H, Daszak P, Eaton BT, Zhang S, Wang LF.** 2005. Bats are natural reservoirs of SARS-like coronaviruses. Science **310**:676–679.
7. **Li W, Zhang C, Sui J, Kuhn JH, Moore MJ, Luo S, Wong SK, Huang IC, Xu K, Vasilieva N, Murakami A, He Y, Marasco WA, Guan Y, Choe H, Farzan M.** 2005. Receptor and viral determinants of SARS-coronavirus adaptation to human ACE2. EMBO J. **24**:1634–1643.
8. **Poon LL, Chu DK, Chan KH, Wong OK, Ellis TM, Leung YH, Lau SK, Woo PC, Suen KY, Yuen KY, Guan Y, Peiris JS.** 2005. Identification of a novel coronavirus in bats. J. Virol. **79**:2001–2009.
9. **Yount B, Roberts RS, Sims AC, Deming D, Frieman MB, Sparks J, Denison MR, Davis N, Baric RS.** 2005. Severe acute respiratory syndrome coronavirus group-specific open reading frames encode nonessential functions for replication in cell cultures and mice. J. Virol. **79**:14909–14922.
10. **Reid SP, Leung LW, Hartman AL, Martinez O, Shaw ML, Carbonnelle C, Volchkov VE, Nichol ST, Basler CF.** 2006. Ebola virus VP24 binds karyopherin alpha1 and blocks STAT1 nuclear accumulation. J. Virol. **80**:5156–5167.
11. **Shaw ML, Cardenas WB, Zamarin D, Palese P, Basler CF.** 2005. Nuclear localization of the Nipah virus W protein allows for inhibition of both virus- and toll-like receptor 3-triggered signaling pathways. J. Virol. **79**:6078–6088.
12. **Porter FW, Palmenberg AC.** 2009. Leader-induced phosphorylation of nucleoporins correlates with nuclear trafficking inhibition by cardioviruses. J. Virol. **83**:1941–1951.
13. **Suzuki T, Yamamoto N, Nonaka M, Hashimoto Y, Matsuda G, Takeshima SN, Matsuyama M, Igarashi T, Miura T, Tanaka R, Kato S, Aida Y.** 2009. Inhibition of human immunodeficiency virus type 1 (HIV-1) nuclear import via Vpr-importin alpha interactions as a novel HIV-1 therapy. Biochem. Biophys. Res. Commun. **380**:838–843.
14. **Shih SR, Stollar V, Li ML.** 2011. Host factors in enterovirus 71 replication. J. Virol. **85**:9658–9666.
15. **Basler CF, Amarasinghe GK.** 2009. Evasion of interferon responses by Ebola and Marburg viruses. J. Interferon Cytokine Res. **29**:511–520.
16. **Chelbi-Alix MK, Vidy A, El Bougrini J, Blondel D.** 2006. Rabies viral mechanisms to escape the IFN system: the viral protein P interferes with IRF-3, Stat1, and PML nuclear bodies. J. Interferon Cytokine Res. **26**:271–280.
17. **Frieman M, Yount B, Heise M, Kopecky-Bromberg SA, Palese P, Baric RS.** 2007. Severe acute respiratory syndrome coronavirus ORF6 antagonizes STAT1 function by sequestering nuclear import factors on the rough endoplasmic reticulum/Golgi membrane. J. Virol. **81**:9812–9824.
18. **Holloway G, Truong TT, Coulson BS.** 2009. Rotavirus antagonizes cellular antiviral responses by inhibiting the nuclear accumulation of STAT1, STAT2, and NF-κB. J. Virol. **83**:4942–4951.
19. **Horner SM, Gale M, Jr.** 2009. Intracellular innate immune cascades and interferon defenses that control hepatitis C virus. J. Interferon Cytokine Res. **29**:489–498.
20. **Schmolke M, Garcia-Sastre A.** 2010. Evasion of innate and adaptive immune responses by influenza A virus. Cell. Microbiol. **12**:873–880.
21. **Chook YM, Suel KE.** 2011. Nuclear import by karyopherin-betas: recognition and inhibition. Biochim. Biophys. Acta **1813**:1593–1606.
22. **Yasmin R, Williams RM, Xu M, Noy N.** 2005. Nuclear import of the retinoid X receptor, the vitamin D receptor, and their mutual heterodimer. J. Biol. Chem. **280**:40152–40160.
23. **Shaulsky G, Goldfinger N, Ben-Ze'ev A, Rotter V.** 1990. Nuclear accumulation of p53 protein is mediated by several nuclear localization signals and plays a role in tumorigenesis. Mol. Cell. Biol. **10**:6565–6577.
24. **Liang SH, Clarke MF.** 1999. The nuclear import of p53 is determined by the presence of a basic domain and its relative position to the nuclear localization signal. Oncogene **18**:2163–2166.
25. **Xiao Z, Latek R, Lodish HF.** 2003. An extended bipartite nuclear localization signal in Smad4 is required for its nuclear import and transcriptional activity. Oncogene **22**:1057–1069.
26. **Miyauchi Y, Michigami T, Sakaguchi N, Sekimoto T, Yoneda Y, Pike JW, Yamagata M, Ozono K.** 2005. Importin 4 is responsible for ligand-independent nuclear translocation of vitamin D receptor. J. Biol. Chem. **280**:40901–40908.
27. **Young JC, Major AT, Miyamoto Y, Loveland KL, Jans DA.** 2011. Distinct effects of importin α2 and α4 on Oct3/4 localization and expression in mouse embryonic stem cells. FASEB J. **25**:3958–3965.
28. **Depping R, Steinhoff A, Schindler SG, Friedrich B, Fagerlund R, Metzen E, Hartmann E, Kohler M.** 2008. Nuclear translocation of hypoxia-inducible factors (HIFs): involvement of the classical importin alpha/beta pathway. Biochim. Biophys. Acta **1783**:394–404.
29. **Hill CS.** 2009. Nucleocytoplasmic shuttling of Smad proteins. Cell Res. **19**:36–46.
30. **Edgar R, Domrachev M, Lash AE.** 2002. Gene Expression Omnibus: NCBI gene expression and hybridization array data repository. Nucleic Acids Res. **30**:207–210.
31. **Yoshikawa T, Hill TE, Yoshikawa N, Popov VL, Galindo CL, Garner HR, Peters CJ, Tseng CT.** 2010. Dynamic innate immune responses of human bronchial epithelial cells to severe acute respiratory syndrome-associated coronavirus infection. PLoS One **5**:e8729. doi:10.1371/journal.pone.0008729.
32. **Fulcher ML, Gabriel S, Burns KA, Yankaskas JR, Randell SH.** 2005. Well-differentiated human airway epithelial cell cultures. Methods Mol. Med. **107**:183–206.

33. **Yount B, Curtis KM, Fritz EA, Hensley LE, Jahrling PB, Prentice E, Denison MR, Geisbert TW, Baric RS.** 2003. Reverse genetics with a full-length infectious cDNA of severe acute respiratory syndrome coronavirus. Proc. Natl. Acad. Sci. U. S. A. **100**:12995–13000.
34. **Roberts A, Deming D, Paddock CD, Cheng A, Yount B, Vogel L, Herman BD, Sheahan T, Heise M, Genrich GL, Zaki SR, Baric R, Subbarao K.** 2007. A mouse-adapted SARS-coronavirus causes disease and mortality in BALB/c mice. PLoS Pathog. **3**:e5. doi:10.1371/journal.ppat.0030005.
35. **Pyrc K, Sims AC, Dijkman R, Jebbink M, Long C, Deming D, Donaldson E, Vabret A, Baric R, van der Hoek L, Pickles R.** 2010. Culturing the unculturable: human coronavirus HKU1 infects, replicates, and produces progeny virions in human ciliated airway epithelial cell cultures. J. Virol. **84**:11255–11263.
36. **Sims AC, Baric RS, Yount B, Burkett SE, Collins PL, Pickles RJ.** 2005. Severe acute respiratory syndrome coronavirus infection of human ciliated airway epithelia: role of ciliated cells in viral spread in the conducting airways of the lungs. J. Virol. **79**:15511–15524.
37. **Donaldson EF, Yount B, Sims AC, Burkett S, Pickles RJ, Baric RS.** 2008. Systematic assembly of a full-length infectious clone of human coronavirus NL63. J. Virol. **82**:11948–11957.
38. **Li C, Bankhead A, III, Eisfeld AJ, Hatta Y, Jeng S, Chang JH, Aicher LD, Proll S, Ellis AL, Law GL, Waters KM, Neumann G, Katze MG, McWeeney S, Kawaoka Y.** 2011. Host regulatory network response to infection with highly pathogenic H5N1 avian influenza virus. J. Virol. **85**:10955–10967.
39. **Cilloniz C, Pantin-Jackwood MJ, Ni C, Goodman AG, Peng X, Proll SC, Carter VS, Rosenzweig ER, Szretter KJ, Katz JM, Korth MJ, Swayne DE, Tumpey TM, Katze MG.** 2010. Lethal dissemination of H5N1 influenza virus is associated with dysregulation of inflammation and lipoxin signaling in a mouse model of infection. J. Virol. **84**:7613–7624.
40. **Dennis G, Jr, Sherman BT, Hosack DA, Yang J, Gao W, Lane HC, Lempicki RA.** 2003. DAVID: Database for annotation, visualization, and integrated discovery. Genome Biol. **4**:P3. doi:10.1186/gb-2003-4-5-p3.
41. **Huang da, W, Sherman BT, Lempicki RA.** 2009. Systematic and integrative analysis of large gene lists using DAVID bioinformatics resources. Nat. Protoc. **4**:44–57.
42. **Nikolsky Y, Kirilov E, Zuez R, Rakhmatulin E, Nikolskaya T.** 2009. Functional anlaysis of OMICs data and small molecule compounds in an integrated "knowledge-baseed" platform, p 177–196. *In* Bryant Y, Na J (ed), Protein networks and pathway analysis, vol 563. Humana Press, Totowa, NJ.
43. **Shannon P, Markiel A, Ozier O, Baliga NS, Wang JT, Ramage D, Amin N, Schwikowski B, Ideker T.** 2003. Cytoscape: a software environment for integrated models of biomolecular interaction networks. Genome Res. **13**:2498–2504.
44. **Metz TO, Jacobs JM, Gritsenko MA, Fontes G, Qian WJ, Camp DG, II, Poitout V, Smith RD.** 2006. Characterization of the human pancreatic islet proteome by two-dimensional LC/MS/MS. J. Proteome Res. **5**:3345–3354.
45. **Petyuk VA, Qian WJ, Hinault C, Gritsenko MA, Singhal M, Monroe ME, Camp DG, II, Kulkarni RN, Smith RD.** 2008. Characterization of the mouse pancreatic islet proteome and comparative analysis with other mouse tissues. J. Proteome Res. **7**:3114–3126.
46. **Zimmer JS, Monroe ME, Qian WJ, Smith RD.** 2006. Advances in proteomics data analysis and display using an accurate mass and time tag approach. Mass Spectrom. Rev. **25**:450–482.
47. **Livesay EA, Tang K, Taylor BK, Buschbach MA, Hopkins DF, LaMarche BL, Zhao R, Shen Y, Orton DJ, Moore RJ, Kelly RT, Udseth HR, Smith RD.** 2008. Fully automated four-column capillary LC-MS system for maximizing throughput in proteomic analyses. Anal. Chem. **80**:294–302.
48. **Kiebel GR, Auberry KJ, Jaitly N, Clark DA, Monroe ME, Peterson ES, Tolic N, Anderson GA, Smith RD.** 2006. PRISM: a data management system for high-throughput proteomics. Proteomics **6**:1783–1790.
49. **Jaitly N, Mayampurath A, Littlefield K, Adkins JN, Anderson GA, Smith RD.** 2009. Decon2LS: an open-source software package for automated processing and visualization of high resolution mass spectrometry data. BMC Bioinformatics **10**:87. doi:10.1186/1471-2105-10-87.
50. **Monroe ME, Tolic N, Jaitly N, Shaw JL, Adkins JN, Smith RD.** 2007. VIPER: an advanced software package to support high-throughput LC-MS peptide identification. Bioinformatics **23**:2021–2023.
51. **Webb-Robertson BJ, McCue LA, Waters KM, Matzke MM, Jacobs JM, Metz TO, Varnum SM, Pounds JG.** 2010. Combined statistical analyses of peptide intensities and peptide occurrences improves identification of significant peptides from MS-based proteomics data. J. Proteome Res. **9**:5748–5756.
52. **Matzke MM, Waters KM, Metz TO, Jacobs JM, Sims AC, Baric RS, Pounds JG, Webb-Robertson BJ.** 2011. Improved quality control processing of peptide-centric LC-MS proteomics data. Bioinformatics **27**:2866–2872.
53. **Webb-Robertson BJ, Matzke MM, Jacobs JM, Pounds JG, Waters KM.** 2011. A statistical selection strategy for normalization procedures in LC-MS proteomics experiments through dataset-dependent ranking of normalization scaling factors. Proteomics **11**:4736–4741.
54. **Polpitiya AD, Qian WJ, Jaitly N, Petyuk VA, Adkins JN, Camp DG, II, Anderson GA, Smith RD.** 2008. DAnTE: a statistical tool for quantitative analysis of -omics data. Bioinformatics **24**:1556–1558.
55. **Mansour AA, Gafni O, Weinberger L, Zviran A, Ayyash M, Rais Y, Krupalnik V, Zerbib M, Amann-Zalcenstein D, Maza I, Geula S, Viukov S, Holtzman L, Pribluda A, Canaani E, Horn-Saban S, Amit I, Novershtern N, Hanna JH.** 2012. The H3K27 demethylase Utx regulates somatic and germ cell epigenetic reprogramming. Nature **488**:409–413.
56. **Zhou H, Ferraro D, Zhao J, Hussain S, Shao J, Trujillo J, Netland J, Gallagher T, Perlman S.** 2010. The N-terminal region of severe acute respiratory syndrome coronavirus protein 6 induces membrane rearrangement and enhances virus replication. J. Virol. **84**:3542–3551.
57. **Knoops K, Kikkert M, Worm SH, Zevenhoven-Dobbe JC, van der Meer Y, Koster AJ, Mommaas AM, Snijder EJ.** 2008. SARS-coronavirus replication is supported by a reticulovesicular network of modified endoplasmic reticulum. PLoS Biol. **6**:e226. doi:10.1371/journal.pbio.0060226.
58. **Zhao J, Legge K, Perlman S.** 2011. Age-related increases in PGD(2) expression impair respiratory DC migration, resulting in diminished T cell responses upon respiratory virus infection in mice. J. Clin. Invest. **121**:4921–4930.
59. **Zhao J, Falcon A, Zhou H, Netland J, Enjuanes L, Perez Brena P, Perlman S.** 2009. Severe acute respiratory syndrome coronavirus protein 6 is required for optimal replication. J. Virol. **83**:2368–2373.
60. **Frieman MB, Chen J, Morrison TE, Whitmore A, Funkhouser W, Ward JM, Lamirande EW, Roberts A, Heise M, Subbarao K, Baric RS.** 2010. SARS-CoV pathogenesis is regulated by a STAT1 dependent but a type I, II and III interferon receptor independent mechanism. PLoS Pathog. **6**:e1000849. doi:10.1371/journal.ppat.1000849.
61. **Ding Y, Wang H, Shen H, Li Z, Geng J, Han H, Cai J, Li X, Kang W, Weng D, Lu Y, Wu D, He L, Yao K.** 2003. The clinical pathology of severe acute respiratory syndrome (SARS): a report from China. J. Pathol. **200**:282–289.
62. **Ding Y, He L, Zhang Q, Huang Z, Che X, Hou J, Wang H, Shen H, Qiu L, Li Z, Geng J, Cai J, Han H, Li X, Kang W, Weng D, Liang P, Jiang S.** 2004. Organ distribution of severe acute respiratory syndrome (SARS) associated coronavirus (SARS-CoV) in SARS patients: implications for pathogenesis and virus transmission pathways. J. Pathol. **203**:622–630.
63. **Akerstrom S, Mirazimi A, Tan YJ.** 2007. Inhibition of SARS-CoV replication cycle by small interference RNAs silencing specific SARS proteins, 7a/7b, 3a/3b and S. Antiviral Res. **73**:219–227.
64. **Kopecky-Bromberg SA, Martinez-Sobrido L, Frieman M, Baric RA, Palese P.** 2007. Severe acute respiratory syndrome coronavirus open reading frame (ORF) 3b, ORF 6, and nucleocapsid proteins function as interferon antagonists. J. Virol. **81**:548–557.
65. **Nadler SG, Tritschler D, Haffar OK, Blake J, Bruce AG, Cleaveland JS.** 1997. Differential expression and sequence-specific interaction of karyopherin alpha with nuclear localization sequences. J. Biol. Chem. **272**:4310–4315.
66. **Pujol G, Soderqvist H, Radu A.** 2002. Age-associated reduction of nuclear protein import in human fibroblasts. Biochem. Biophys. Res. Commun. **294**:354–358.
67. **Perlman S, Dandekar AA.** 2005. Immunopathogenesis of coronavirus infections: implications for SARS. Nat. Rev. Immunol. **5**:917–927.
68. **Tangudu C, Olivares H, Netland J, Perlman S, Gallagher T.** 2007. Severe acute respiratory syndrome coronavirus protein 6 accelerates murine coronavirus infections. J. Virol. **81**:1220–1229.
69. **Kim SW, Hong JS, Ryu SH, Chung WC, Yoon JH, Koo JS.** 2007. Regulation of mucin gene expression by CREB via a nonclassical retinoic acid signaling pathway. Mol. Cell. Biol. **27**:6933–6947.
70. **Barlow CA, Barrett TF, Shukla A, Mossman BT, Lounsbury KM.** 2007. Asbestos-mediated CREB phosphorylation is regulated by protein kinase

A and extracellular signal-regulated kinases 1/2. Am. J. Physiol. Lung Cell. Mol. Physiol. **292**:L1361–L1369.
71. **George CL, Fantuzzi G, Bursten S, Leer L, Abraham E.** 1999. Effects of lisofylline on hyperoxia-induced lung injury. Am. J. Physiol. **276**:L776–L785.
72. **Shaheen SO, Jameson KA, Robinson SM, Boucher BJ, Syddall HE, Sayer AA, Cooper C, Holloway JW, Dennison EM.** 2011. Relationship of vitamin D status to adult lung function and COPD. Thorax **66**:692–698.
73. **Sundar IK, Hwang JW, Wu S, Sun J, Rahman I.** 2011. Deletion of vitamin D receptor leads to premature emphysema/COPD by increased matrix metalloproteinases and lymphoid aggregates formation. Biochem. Biophys. Res. Commun. **406**:127–133.
74. **Song Y, Kato S, Fleet JC.** 2003. Vitamin D receptor (VDR) knockout mice reveal VDR-independent regulation of intestinal calcium absorption and ECaC2 and calbindin D9k mRNA. J. Nutr. **133**:374–380.
75. **Percy MJ, Furlow PW, Lucas GS, Li X, Lappin TR, McMullin MF, Lee FS.** 2008. A gain-of-function mutation in the HIF2A gene in familial erythrocytosis. N. Engl. J. Med. **358**:162–168.
76. **Smits SL, de Lang A, van den Brand JM, Leijten LM, van IWF, Eijkemans MJ, van Amerongen G, Kuiken T, Andeweg AC, Osterhaus AD, Haagmans BL.** 2010. Exacerbated innate host response to SARS-CoV in aged non-human primates. PLoS Pathog. **6**:e1000756. doi:10.1371/journal.ppat.1000756.
77. **Rockx B, Feldmann F, Brining D, Gardner D, LaCasse R, Kercher L, Long D, Rosenke R, Virtaneva K, Sturdevant DE, Porcella SF, Mattoon J, Parnell M, Baric RS, Feldmann H.** 2011. Comparative pathogenesis of three human and zoonotic SARS-CoV strains in cynomolgus macaques. PLoS One **6**:e18558. doi:10.1371/journal.pone.0018558.
78. **Carlson CM, Turpin EA, Moser LA, O'Brien KB, Cline TD, Jones JC, Tumpey TM, Katz JM, Kelley LA, Gauldie J, Schultz-Cherry S.** 2010. Transforming growth factor-beta: activation by neuraminidase and role in highly pathogenic H5N1 influenza pathogenesis. PLoS Pathog. **6**:e1001136. doi:10.1371/journal.ppat.1001136.
79. **Tong XD, Liu HX, Zhao HR, Xu SG, Li Y, Han LB, Zhang L.** 2006. The role of Smad4 and MAPK proteins in signal transduction pathway in non-small cell lung cancer. Zhonghua Zhong Liu Za Zhi. **28**:741–745. (In Chinese.)
80. **Munoz-Fontela C, Macip S, Martinez-Sobrido L, Brown L, Ashour J, Garcia-Sastre A, Lee SW, Aaronson SA.** 2008. Transcriptional role of p53 in interferon-mediated antiviral immunity. J. Exp. Med. **205**:1929–1938.
81. **Turpin E, Luke K, Jones J, Tumpey T, Konan K, Schultz-Cherry S.** 2005. Influenza virus infection increases p53 activity: role of p53 in cell death and viral replication. J. Virol. **79**:8802–8811.
82. **Sato Y, Kamura T, Shirata N, Murata T, Kudoh A, Iwahori S, Nakayama S, Isomura H, Nishiyama Y, Tsurumi T.** 2009. Degradation of phosphorylated p53 by viral protein-ECS E3 ligase complex. PLoS Pathog. **5**:e1000530. doi:10.1371/journal.ppat.1000530.
83. **Dobbelstein M, Roth J.** 1998. The large T antigen of simian virus 40 binds and inactivates p53 but not p73. J. Gen. Virol. **79**:3079–3083.
84. **Chen Y, Chan VS, Zheng B, Chan KY, Xu X, To LY, Huang FP, Khoo US, Lin CL.** 2007. A novel subset of putative stem/progenitor CD34+Oct-4+ cells is the major target for SARS coronavirus in human lung. J. Exp. Med. **204**:2529–2536.
85. **Chang CC, Shieh GS, Wu P, Lin CC, Shiau AL, Wu CL.** 2008. Oct-3/4 expression reflects tumor progression and regulates motility of bladder cancer cells. Cancer Res. **68**:6281–6291.
86. **Malhotra D, Portales-Casamar E, Singh A, Srivastava S, Arenillas D, Happel C, Shyr C, Wakabayashi N, Kensler TW, Wasserman WW, Biswal S.** 2010. Global mapping of binding sites for Nrf2 identifies novel targets in cell survival response through ChIP-Seq profiling and network analysis. Nucleic Acids Res. **38**:5718–5734.
87. **Waters KM, Pounds JG, Thrall BD.** 2006. Data merging for integrated microarray and proteomic analysis. Brief Funct. Genomic Proteomic. **5**:261–272.
88. **McDermott JE, Shankaran H, Eisfeld AJ, Belisle SE, Neuman G, Li C, McWeeney S, Sabourin C, Kawaoka Y, Katze MG, Waters KM.** 2011. Conserved host response to highly pathogenic avian influenza virus infection in human cell culture, mouse and macaque model systems. BMC Syst. Biol. **5**:190. doi:10.1186/1752-0509-5-190.
89. **Rockx B, Sheahan T, Donaldson E, Harkema J, Sims A, Heise M, Pickles R, Cameron M, Kelvin D, Baric R.** 2007. Synthetic reconstruction of zoonotic and early human severe acute respiratory syndrome coronavirus isolates that produce fatal disease in aged mice. J. Virol. **81**:7410–7423.
90. **Zornetzer GA, Frieman MB, Rosenzweig E, Korth MJ, Page C, Baric RS, Katze MG.** 2010. Transcriptomic analysis reveals a mechanism for a pre-fibrotic phenotype in STAT1 knockout mice during severe acute respiratory syndrome coronavirus infection. J. Virol. **84**:11297–11309.